Journal of Nuclear Materials 619 (2026) 156250

Contents lists available at ScienceDirect

Journal of Nuclear Materials

journal homepage: www.elsevier.com/locate/jnucmat

Hydride morphology in zirconium cladding tubes after the SPIZWURZ bundle test. Part I: analysis of experimental data

Mikhail Kolesnik *, Juri Stuckert, Mirco Grosse, Sarah Weick

Institute for Applied Materials – Applied Material Physics (IAM-AWP), Karlsruhe Institute of Technology, Karlsruhe, Germany

ARTICLE INFO

Keywords:
Zirconium alloys
Hydride morphology
Hydride embrittlement
Dry storage
Spent nuclear fuel
Hydride reorientation

ABSTRACT

The SPIZWURZ bundle test was carried out at the LICAS facility at Karlsruhe Institute of Technology. The test involved a bundle of 21 unirradiated hydrogenated cladding tubes (Zircaloy-4, opt. ZIRLO™ and Duplex DX-D4) which were subjected to an internal gas pressure and slow cooling for 250 days simulating the dry storage conditions of spent nuclear fuel. The following hydride morphology metrics were measured after the test: radial hydride fraction; hydride continuity coefficient; hydride length (mean and maximum, and their statistical distributions and densities); and number density. Hydrides in Zircaloy-4 have a higher tendency to reorientation, higher connectivity and are 2–3 times shorter (in both maximal and mean length) than those in opt. ZIRLO™. The evolution of hydride morphology in DX-D4 is mainly characterized by diffusional redistribution of hydrides from the substrate to the liner and the liner/substrate interface. Several samples exhibited local anomalies in hydride morphology, which can cause significant local embrittlement. The main experimental results are in good agreement with earlier published data. The supplementary materials include records of all the thermocouples and pressure sensors, which can be used to simulate the SPIZWURZ bundle test in detail.

1. Introduction

The current concept for managing spent nuclear fuel (SNF) in Germany envisages dry storage (DS) in dual-purpose casks as an interim solution until final disposal in a stable geological formation, which could be possible after 2060. During DS, the physical conditions are characterized 1) by self-heating of the fuel due to decay heat in the pellets, and 2) by gas pressure inside the rod cladding due to the initial inner pressure, the high temperature and the release of fission gases (mainly during operation). The temperature of the SNF reaches its maximum at the beginning of the DS period and then slowly decreases as the decay heat naturally reduces. The main risks to SNF integrity during DS are cladding creep [1–3] and hydrogen-induced degradation of the cladding's mechanical properties due to hydrogen redistribution and hydride morphology changes [4,5]. These physical mechanisms have been investigated experimentally in the context of the SPIZWURZ project.

SPIZWURZ (an acronym for the German title Spannungsinduzierte Wasserstoffumlagerung während Langzeit-Zwischenlagerung, meaning stress-induced hydrogen redistribution during long-term intermediate storage) is a collaborative project between the Gesellschaft für Anlagen- und Reaktorsicherheit (GRS) and two institutes of the Karlsruhe Institute of Technology (KIT): the Institute for Applied Materials – Applied Materials Physics (IAM-AWP) and the Institute for Nuclear Waste Disposal (INE) [6,7]. The experimental part of the project involved testing of 21 hydrogenated industrial cladding tubes assembled in a bundle and subjected to a thermalomechanical scenario that simulated dry storage conditions [6,7]. This test was carried out at the LICAS facility at KIT. The SPIZWURZ bundle test is unique in its long-sized samples (2.5 m) and long cooling period of 250 days. This paper discusses the results of hydride morphology measurements in cladding tubes after the bundle test and compares them with earlier published data.

2. SPIZRWURZ bundle test

2.1. Experiment description

The test sample bundle included twenty-one unirradiated pre-hydrogenated industrial cladding tubes, each 2.5 m long and made of stress relieved annealed (SRA) Zircaloy-4, partially recrystallized (pRXA) opt. ZIRLO™ and duplex alloy DX-D4 (SRA), consisting of an inner Zircaloy-4 substrate layer (thickness approximately 600 μm) and an external liner layer (approximately 150 μm [8,9]). The chemical

* Corresponding author.
E-mail address: m.kolesnik@kit.edu (M. Kolesnik).

https://doi.org/10.1016/j.jnucmat.2025.156250
Received 25 July 2025; Received in revised form 20 October 2025; Accepted 27 October 2025
Available online 28 October 2025

composition of allots is in Table 1. The cladding tubes were filled by annular pellets made of ZrO_2 stabilized by yttria. Each test rod was heated by a tungsten heater passing through the center of the annular pellets. Each rod was individually pressurized with a krypton/oxygen gas mixture. Throughout the experiment, the bundle was kept in an argon/oxygen atmosphere and covered with a thermally insulated shroud. The bundle's cross-section is shown in Fig. 1. Rods 1, 5 and 14 were each equipped with 15 thermocouples attached to the outer surface of the cladding at different bundle elevations. Additional thermocouples were placed inside the corner rods made of Zircaloy-4 (15 thermocouples in total) and on the outer surface of the zirconium shroud (13 thermocouples in total).

In the SPIZWURZ bundle test, the temperature and stress conditions were designed to reproduce the DS environment of SNF. The bundle was heated to 400 °C (the maximum cladding temperature allowed in dry storage by the U.S. Nuclear Regulatory Commission [10]) and subsequently cooled stepwise over 250 (Fig. 2). The temperature profiles along the rods at the beginning and end of the test, as recorded by the thermocouples, are shown in Fig. 3 (the axial zero level corresponds to the start of the main heat generation in the rods). The internal gas pressure was set independently for each test rod with two target values: 106 and 146 bar. This was maintained at a constant level throughout the test, as can be seen in Fig. 4. Minor pressure fluctuations (10 – 20 bar) were due to slow cool down, gas leakage and regular compensation. Significant drops in gas pressure and temperature occurred due to several blackouts during the experiment. Power blackouts may potentially influence the experimental results; however, their overall impact is assumed to be limited. In samples and axial zones where complete dissolution of hydrides occurs after reheating to the target temperature, the effect is negligible and may only be relevant to the weak hydride memory effect. In samples and zones with partial hydride dissolution, the influence is less straightforward. Nevertheless, we consider it to be minor, since the temperature drop during a blackout is rapid compared with the experimental heating regimes and may only induce precipitation of small hydrides at high-energy nucleation sites. Upon subsequent reheating, these newly formed small hydrides are expected to dissolve preferentially. Consequently, the final microstructure after heating should remain close to that existing prior to the blackout, and the net effect is weak. Records of all thermocouples and gas pressure control devices can be found in the supplementary materials for this paper in the files "SPIZWURZ_temperature.xlsx" and "SPIZWURZ_pressure.xlsx".

The hoop stresses in the cladding can be estimated using the simplified thin-walled cylinder approximation as:

$$\sigma_\theta = P\frac{R_{ci}}{h_c} \tag{1}$$

where P is the internal gas pressure, R_{ci} is the internal radius of the cladding (4.65 mm) and h_c is the thickness of the cladding (0.725 mm). Eq. (1) provides a reliable estimate of the average hoop stress approximately at mid-thickness. For the given geometry, the variation of hoop stress across the cladding wall is about 13 – 15 %, according to the Lame solution for a thick-walled cylinder.

2.2. Hydrogen charging

Before the SPIZWURZ bundle test, the cladding tubes were precharged with hydrogen from the gas phase through the inner cladding surface in a dedicated furnace at approximately 450 °C for up to 8 h [11]. According to the correlation describing the recrystallization kinetics in Zircaloy-4 reported in [12] ($F = F_0 \cdot \exp(-2.08 \cdot 10^{18} \cdot t \cdot \exp(-41,550/T))$, where F – unrecrystallized fraction, $F_0 = 1$ – initial unrecrystallized fraction, t – time (s), T – absolute temperature), the volume fraction of recrystallized material under these hydrogenation conditions is expected to remain below 1 %. This negligible degree of recrystallization is further supported by experimental observations [13], which showed no detectable changes in grain structure after annealing at 450 °C for durations shorter than 24 h. Consequently, no measurable recrystallization is anticipated during the hydrogen charging step.

Two target values of hydrogen content were defined: 100 ppm and 300 ppm. The samples were hydrogenated by repeatedly exposing them to a cycle of regular hydrogen injections into the surrounding atmosphere. As can be seen in Fig. 5, the charging rates of the various alloys differed significantly for a single injection cycle: Zircaloy-4 and DX-D4 charged around two times faster than opt. ZIRLO.

Fig. 6 shows the scatter of the real values at different axial zones. All data were measured using the gas extraction method after the bundle test. This experimental data is also available in the supplementary materials file "SPIZWURZ_hydrogen.xlsx".

The adsorption of hydrogen from a gaseous state onto the surface of a zirconium alloy involves three steps: (1) dissociation of the hydrogen molecule and adsorption of hydrogen atoms by the zirconium surface; (2) lateral interaction between atoms on the two-dimensional surface; and (3) an adsorbed hydrogen atom jumping into an interstitial site and diffusing in the metal bulk as an interstitial atom [14]. According to [15], the adsorption kinetics are governed by surface adsorption and dissociation at temperatures below 600 °C, and by volume diffusion at temperatures above 600 °C (for gaseous deuterium and Zr-2.5Nb). Therefore, surface adsorption is expected to be the limiting mechanism in experimental conditions.

Opt. ZIRLO and Zircaloy-4 differ in their concentrations of alloying elements, as can be seen in Table 1. Zircaloy-4 contains higher concentrations of Fe and Cr, resulting in a higher number of intermetallide inclusions (also termed as secondary phase particles or SPP). Laves phases are known for their highly effective adsorption of hydrogen from the gaseous phase [16,17–19] and Zr-rich Zr_2Fe is used to trap hydrogen isotopes [20,21]. Second-phase particles can also act as "bridges" that allow hydrogen to pass through the thin oxide layer on the surface [22,23]. It could be therefore assumed that the Laves phases on the surface contribute to the adsorption of gaseous hydrogen, making the adsorption rate of Zircaloy-4 faster than that of opt. ZIRLO. However, the exact physical mechanism remains unclear.

Table 1
Chemical composition of cladding tube materials used in the experiment.

Alloying elements, [wt %]	Sn	Fe	Cr	Nb	O
SRA Zircaloy-4, D4 (substrate)	1.3	0.2	0.1	–	0.13
pRXA opt. ZIRLO	0.8	0.1	–	1.0	–
DX (liner,)	0.5	0.5	0.2	–	0.14

3. Experimental results and analysis

3.1. Hydride morphology determination with special numerical tool

The following hydride morphology parameters were measured in the samples after the SPIZWURZ bundle test: Radial Hydride Fraction (RHF), Hydride Continuity Coefficient (HCC), Radial Hydride Continuity Path (RHCP), maximum length of hydrides (among all and radial only), mean length of hydrides (among all, circumferential and radial), hydride length density (the total length of the hydrides in a selected region of the micrograph divided by the area of that region), surface number density of hydrides, and parameters of the statistical distribution of hydride lengths. These measurements were taken at different elevations of each cladding tube within the bundle.

Here, RHF is defined as the ratio of the total length of the radial hydrides to that of all the hydrides:

$$\mathrm{RHF} = \frac{\sum_{i=1}^{n} l_{r,i}}{\sum_{j=1}^{m} l_j} \tag{2}$$

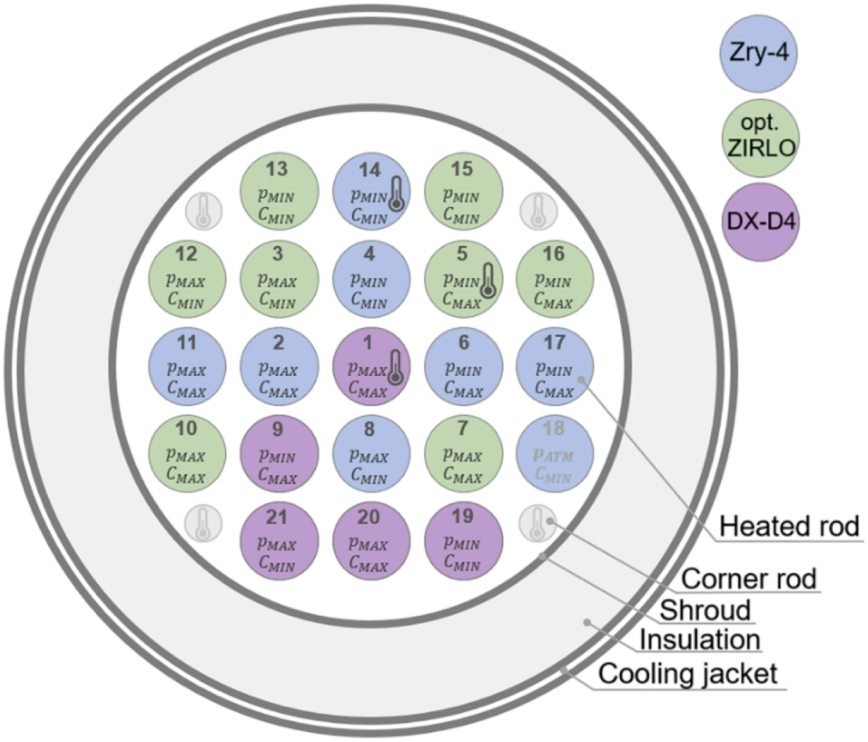

Fig. 1. Cross-section of the SPIZWURZ bundle with indication of pressurization state (p_{MAX}, p_{MIN}), hydrogen concentration (C_{MAX}, C_{MIN}) and positions of thermocouples.

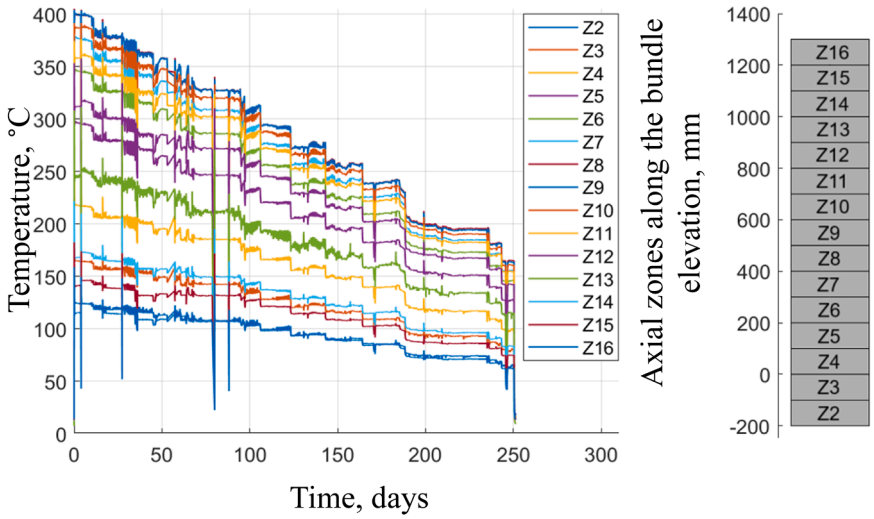

Fig. 2. Temperature scenario in the central rod (rod 1) of the bundle in different axial zones (Z2 – Z16).

where $l_{r,i}$ is the length of the i th radial hydride (oriented at an angle of >45° to the circumferential direction), l_j is the length of the j-th hydride (radial or circumferential), n is the number of radial hydrides, m is the total number of hydrides in the selected area.

The micrographs processing involved manual and numerical stages. During the manual stage, the hydrides in the images were outlined using an image analysis software to increase the contrast and remove visual noise resulting from mechanical treatment and acid etching of the section surface. This noise would otherwise be included in the numerical analysis. This stage is illustrated in Fig. 7. According to ASTM standard specification B811 [24], only hydride platelets measuring >15 μm in length or extending >15 μm in the secondary direction were considered. In the second stage, images containing only outlined hydrides (see Fig. 7c) were processed using a numerical tool described in [25] to evaluate the RHF.

RHCP was first introduced in [25] to characterize the relative reduction in fracture energy for a given hydride morphology compared to a sample without hydrides. RHCP is defined as the maximum estimated relative fracture energy reduction among all possible crack paths.

$$\mathrm{RHCP} = \max\left(\frac{(L - x_{\mathrm{Zr}})w_{\mathrm{Zr}} - x_{\mathrm{ZrH}} \cdot w_{\mathrm{ZrH}}}{L(w_{\mathrm{Zr}} - w_{\mathrm{ZrH}})}\right) \tag{3}$$

where L is the width of the processing image (which is potentially equal to the cladding thickness), x_{Zr} and x_{ZrH} are the path lengths in the zirconium and hydride phases for a given crack path, and w_{Zr} and w_{ZrH} are the penalties associated with the zirconium and hydride phases (i.e.

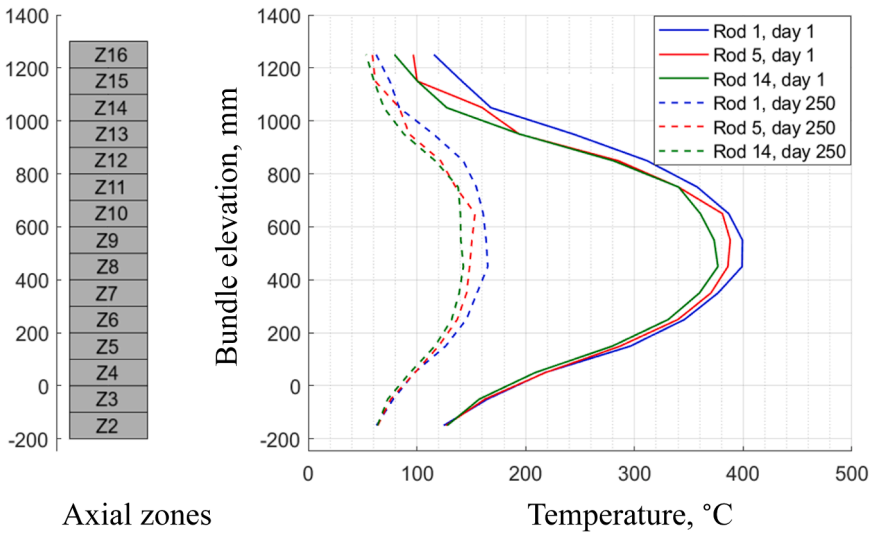

Fig. 3. Axial temperature profiles on day 1 and day 250 for three rods equipped with thermocouples (right), and a diagram showing the numbering of the axial zones and thermocouples (left).

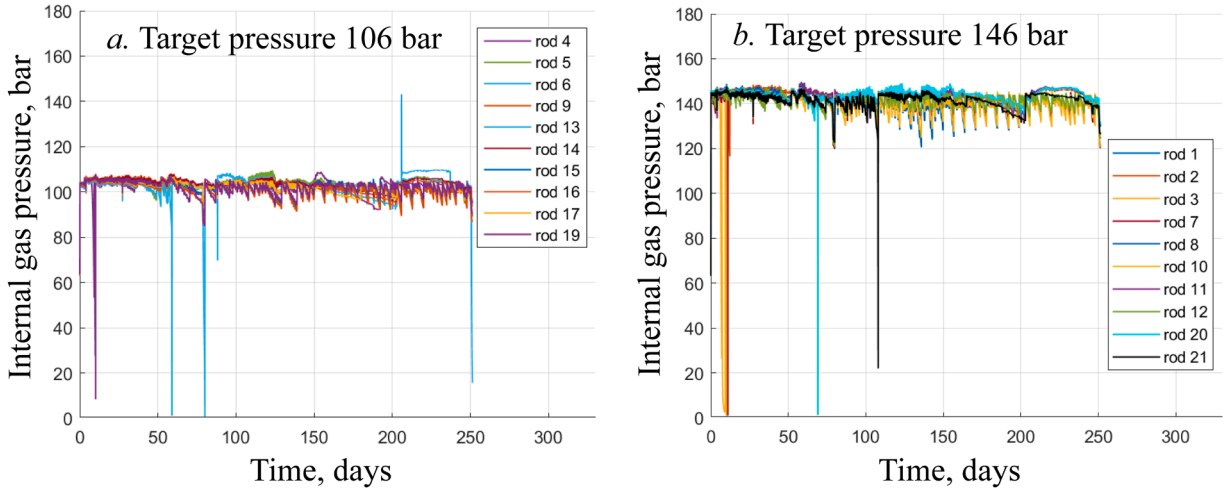

Fig. 4. The internal gas pressure scenario in each rod (excluding rod 18, the witness sample, which was not loaded). The hoop stresses corresponding to the target pressures of 106 and 146 bar are estimated to be 68 and 93 MPa, respectively.

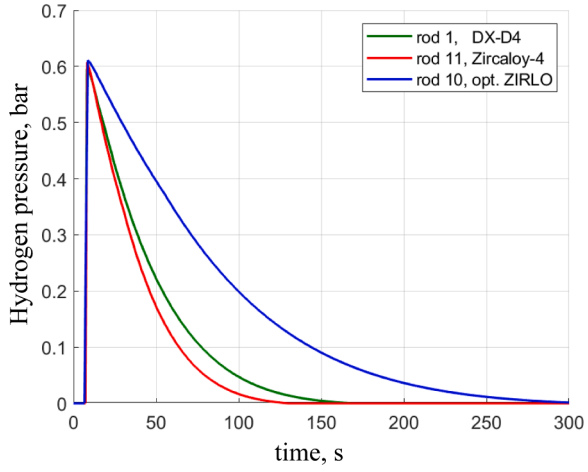

Fig. 5. The hydrogen adsorption rate differs significantly in different zirconium alloys.

fracture toughness). RHCP is estimated using the identical numerical tool on the same manually processed images that were used to estimate the RHF (see Fig. 7*c* for an example).

According to [25] and [26], HCC is the sum of hydride length projected on the radial direction in a band with 110 μm wide in a circumferential direction, normalized by the length of the band (similar to accumulated hydride length AHL defined in [27]). HCC was estimated for each micrograph as the maximal value in a band with maximum projection length of radial hydrides (the "worst" area with the highest local embrittlement), when it was applicable.

For hydride length analysis, the micrograph area containing >200 hydrides (relevant for statistical analysis) was selected first. Then, the lengths of all the hydrides in the selected area were measured. Finally, statistics of the hydride lengths were analyzed to estimate mean and maximum hydride lengths, length density and numerical density, as well as the parameters of statistical length distributions. The hydride length data was also used to provide an alternative estimation of RHF validation of the main method described above.

The measured values of the hydride morphology metrics are presented in two tables in the Appendix.

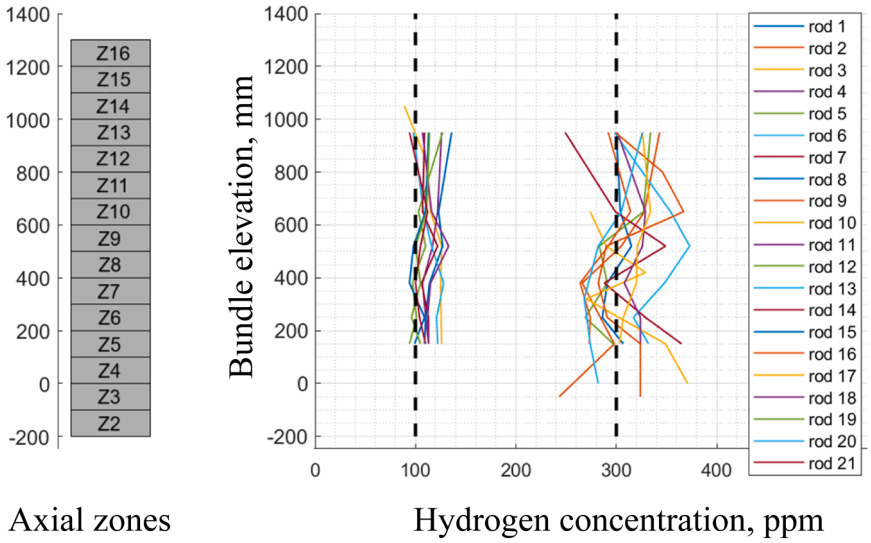

Fig. 6. The axial profiles of hydrogen concentration in all samples after the bundle test. There were two target hydrogen concentrations: 100 ppm and 300 ppm.

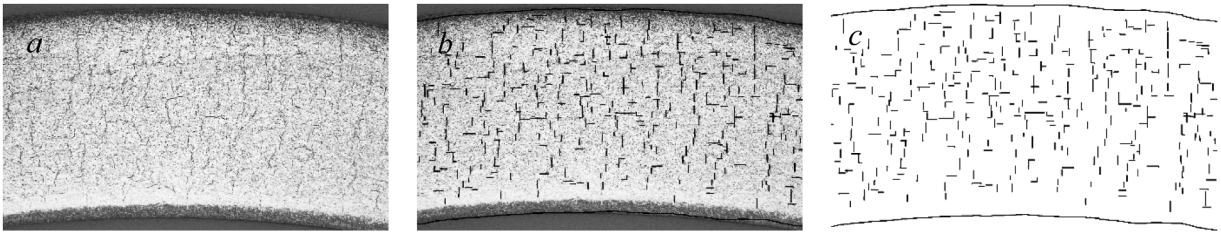

Fig. 7. An example of the manual part of the micrograph processing (rod 8, elevation 520 mm, angle 0°); *a* – original image, *b* – the original image with outlined hydrides, *c* – outlined hydrides only (used for further numerical analysis).

3.2. Analysis of RHF measurement results

The measured RHF in the hot axial zones (at the bundle elevations of 300–700 mm) of all samples manufactured from Zircaloy-4 and opt. ZIRLO™, after the SPIZWURZ bundle test, has been compared with earlier published data for Zircaloy-4 (both Cold Worked Stress Relieved (CWSR) and Stress Relief Annealed (SRA)) and ZIRLO. The list of experiments and their main features is provided in Table 2. The comparison was carried out separately for samples with almost complete (around 100 %) and partial (around 50 %) dissolution of hydrides, as shown in Figs. 8 and 9. This comparison should be considered approximate as the parameters of the experiments may differ slightly (e.g. cooling rate, hydrogen concentration, maximum temperature, stress dependence on time during cooling, RHF measurement procedure, etc.). Nevertheless, it can be postulated that, within the margin of error, the results of the SPIZWURZ bundle test agree well with other published results and RHF growth with hoop stresses.

Table 2
Main parameters of the experiments used for comparison with the SPIZWURZ bundle test.

Reference	alloy	loading scheme	stress when cooling	Comment
SPIZWURZ bundle test	opt. ZIRLO	gas-filled tubes	constant	
	CWSR Zircaloy-4	gas-filled tubes	constant	
Auzoux et al. [28]	ZIRLO	gas-filled tubes	constant	RHF for all the unirradiated samples has been estimated here from the micrographs in [28]
	CWSR Zircaloy-4	gas-filled tubes	constant	
Desquines et al. [29]	SRA Zircaloy-4	gas-filled tubes	constant	only one sample with constant stresses during cooling
Chu et al. [30]	SRA Zircaloy-4	gas-filled tubes	constant	samples after one cycle only
Kim et al. [31]	CWSR Zircaloy-4	sealed tubes	natural decrease*	RHF in sample 137 ppm at 150 MPa has been estimated here from the micrograph in [31]

* natural decrease – a decrease in stress that is proportional to the absolute temperature.

The data scatter for Zircaloy-4 with complete hydride dissolution (Fig. 8*a*) seems relatively wide, and the SPIZWURZ data at 93 MPa appear overestimated. It should be noted that three points, corresponding to 93 MPa, relate to the hot zones of rod 8, where the pellet imitators came into contact with the cladding and experienced high plastic deformation. The reason for this is probably the increased coefficient of thermal expansion of the ZrO_2 pellets used in this test compared to that of the cladding tube (12×10^{-6}/K for pellet vs. 10.8×10^{-6}/K). This could lead to pellet-cladding interaction and higher stresses in the cladding. SPIZWURZ data for samples with partial hydride dissolution (Fig. 8*b*) are within the scatter range of the published data.

If we compare Figs. 8 and 9, we can see that the scatter of RHF data for ZIRLO and opt. ZIRLO is lower than the scatter of Zircaloy-4 data. The SPIZWURZ data is in acceptable agreement with the published data [28] for unirradiated ZIRLO.

The SPIZWURZ bundle test revealed a higher tendency for hydride reorientation in the Zircaloy-4 than in opt. ZIRLO. This agrees with micrographs of the unirradiated samples in [28] (note that the RHF of the unirradiated samples in [28] has been measured here from the micrographs in Figs. 3, 6 and 7 of [28]). According to data from SPIZWURZ

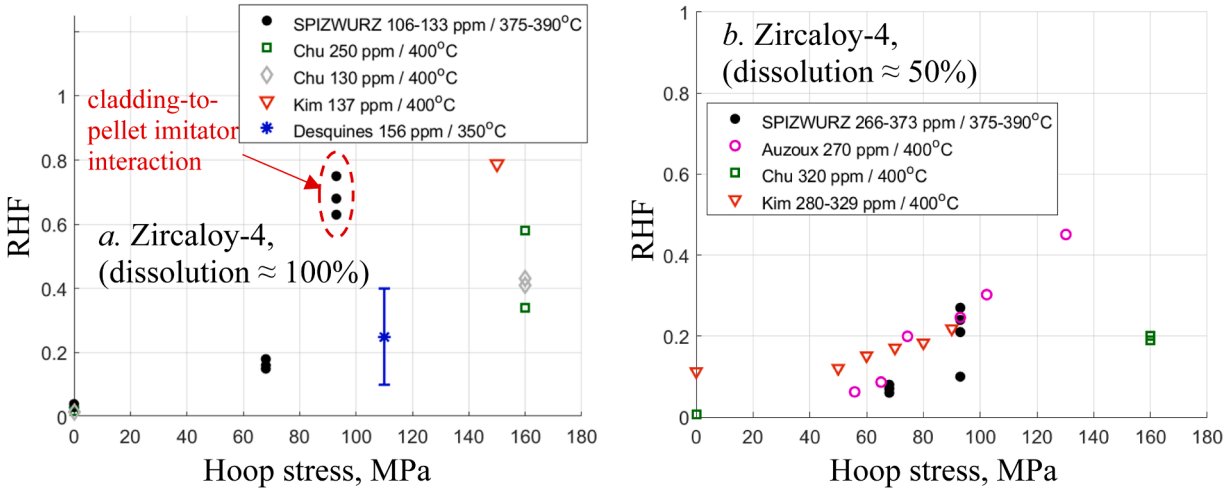

a. Zircaloy-4,(dissolution ≈ 100 %)a. Zircaloy-4,(dissolution ≈ 100 %)Fig. 8. A comparison of the RHF in Zircaloy-4 after hydride reorientation tests.

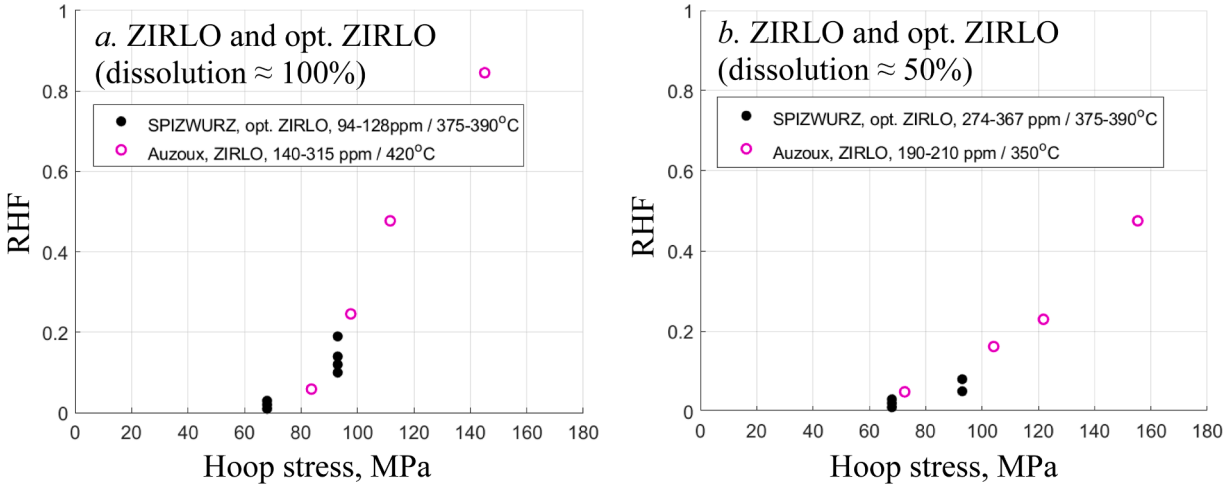

Fig. 9. A comparison of the RHF in ZIRLO and opt. ZIRLO after hydride reorientation test.

and [28], the alloy effect is equal to the shift of the reorientation curve (the RHF vs. hoop stress dependence) for 10–20 MPa, as can be seen in Fig. 10.

The total scatter of all the experimental data in Fig. 10*a* is relatively high, which may hide the effect of the alloy. A more precise comparison, based on SPIZWURZ data only and excluding the uncertainty of hydrogen concentration, maximum temperature, image processing and other factors, can be seen in Fig. 11–14. As can be seen, for all possible

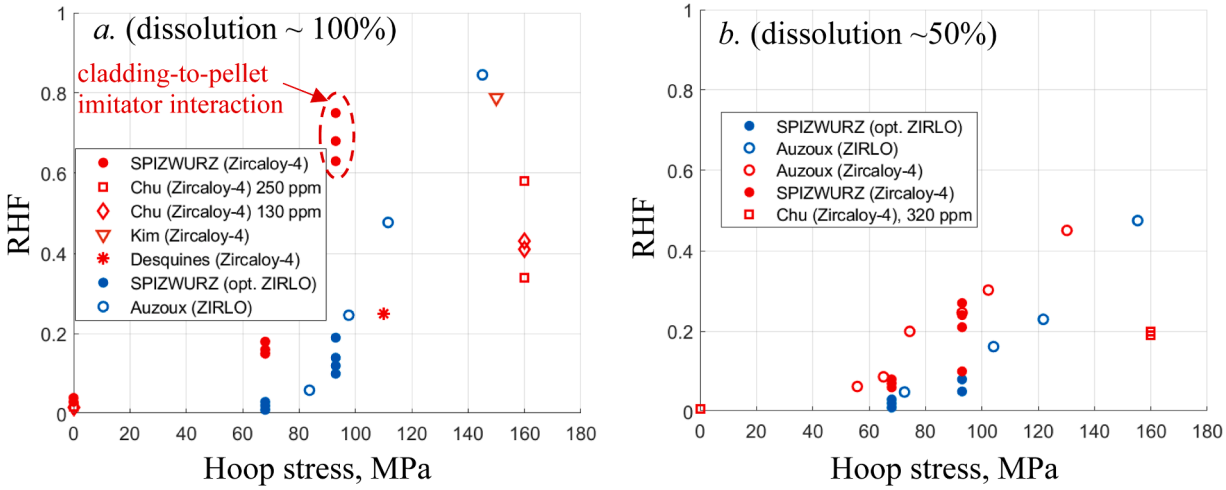

Fig. 10. A comparison of RHF data for Zircaloy-4 (red markers) and ZIRLO/opt. ZIRLO (blue markers).

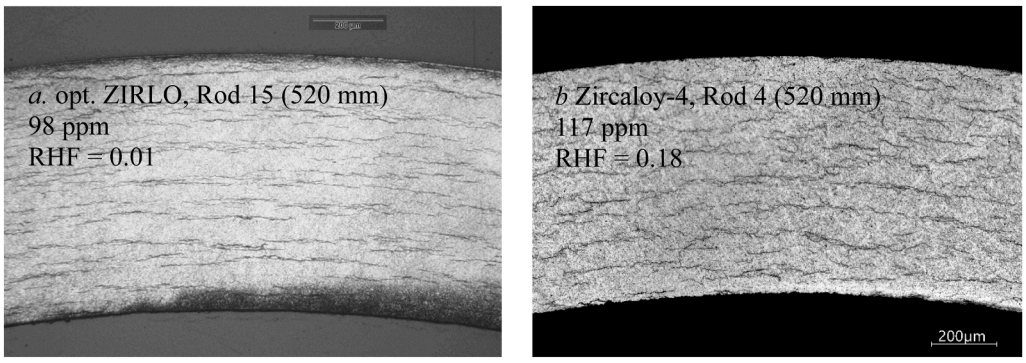

Fig. 11. Hydride morphology in samples with C_{min} and P_{min}.

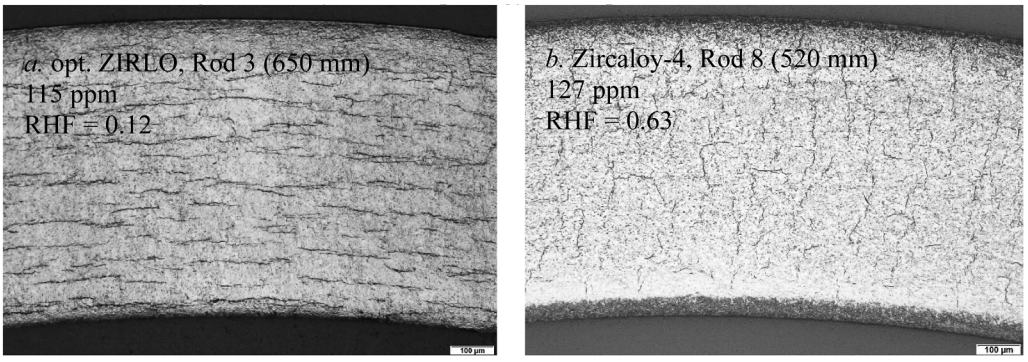

Fig. 12. Hydride morphology in samples with C_{min} and P_{max}.

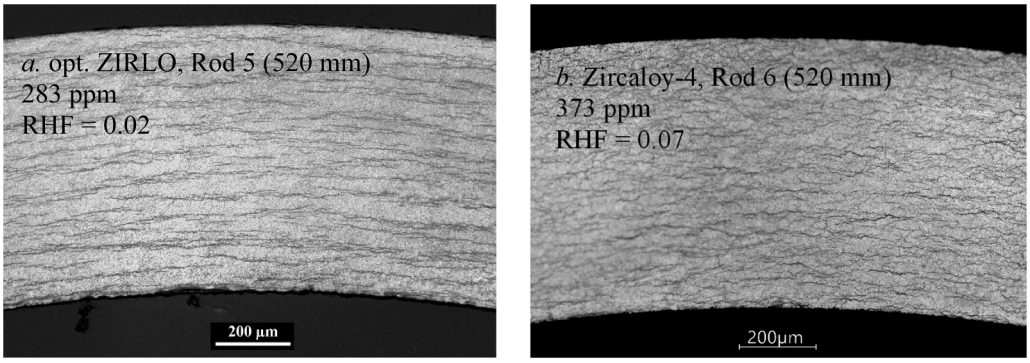

Fig. 13. Hydride morphology in samples with C_{max} and P_{min}.

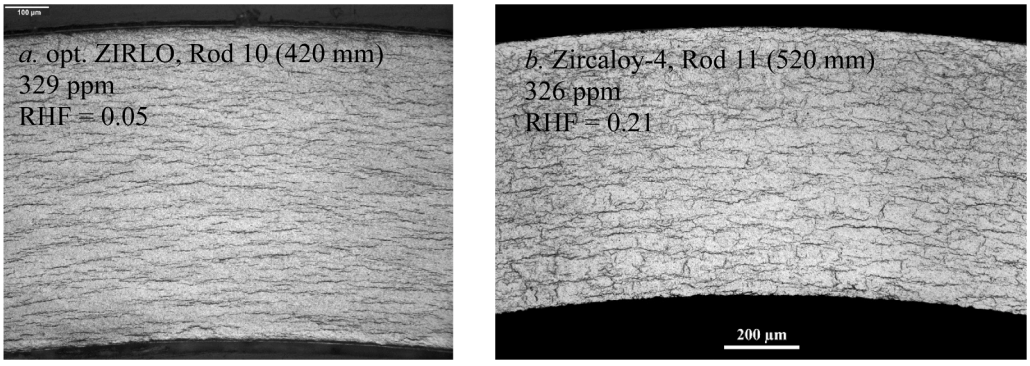

Fig. 14. Hydride morphology in samples with C_{max} and P_{max}.

combinations of hydrogen concentrations (C_{max}, C_{min}) and internal gas pressures (P_{max}, P_{min}), the RHF in Zircaloy-4 is higher than in the opt. ZIRLO.

Note that the above analysis only considers data from unirradiated samples. The degree to which the irradiation factor acts can vary between alloys and potentially change the outcome.

According to [28] and [32], the reorientation stress threshold in Zircaloy-4 cladding for SNF with a high burnup is similar to that of unirradiated tubes, within the margin of error of the experiments. However, nuclear fuel operation leads not only to neutron irradiation, but also to the production of a strong hydrogen concentration gradient in the radial direction of the cladding and hydride rim layer at high burnups, which increases the uncertainty. The pure effect of neutron irradiation on pre-hydrogenated samples in the research reactor gave the opposite result in [33]: the RHF in irradiated Zircaloy-4 (up to fluence $7.5{\cdot}10^{24}$ n/m^2) was lower than in unirradiated Zircaloy-4 (from 0.55 to 0.33 for 250 ppm and from 0.40 to 0.25 for 500 ppm after a reorientation test at a maximum temperature of 400 °C with constant stresses of 150 MPa).

In 1.0Nb-containing alloys, the effects of normal in-reactor operations can be more pronounced and detrimental. According to reference [34], irradiating M5 (spent fuel cladding) reduces the hydride reorientation threshold from approximately 75 MPa (unirradiated) to approximately 50 MPa (irradiated). Irradiated M5 samples reached almost full reorientation at around 130 MPa [34]. Similar results are obtained by comparing experimental data for unirradiated and irradiated (spent fuel cladding) E110 samples, as published in [35] and [36] (almost full reorientation of hydrides in irradiated E110 under 100 MPa [36]). The strong irradiation effect in another 1.0Nb-containing alloy could explain the discrepancy between the SPIZWURZ data for the unirradiated opt. ZIRLO samples and irradiated samples, if compare with data presented in [37] (almost full reorientation of hydrides in irradiated opt. ZIRLO under 100 MPa in [37]).

3.3. Hydride continuity (RHCP and HCC)

The measured hydride continuity metrics, RHCP and HCC, exhibit similar behavior to RHF in response to external stresses within the SPIZWURZ experimental conditions range. Both grow with external stresses, with a slightly higher values in Zircaloy-4 compared to the opt. ZIRLO, as seen in Figs. 15 and 16 (apparently, due to higher reorientation in Zircaloy-4). The mean values of RHCP and HCC at 100 ppm are slightly higher than at 300 ppm. However, it can be expected that, at higher concentrations (above 500 ppm), the connectivity of the hydride network will grow with the hydrogen concentration (as can be seen in Fig. A-1*d* in [38] for RHCP).

Table A1

3.4. Hydride length and surface density

For the hydride length analysis, eight tubes representing all possible combinations of target hydrogen content (100 and 300 ppm) and internal gas pressure (106 and 146 bar) in two alloy tubes (Zircaloy-4 and opt. ZIRLO) were chosen. During the test, all four tubes for each alloy were located axially symmetrically in the bundle, ensuring the same temperature scenario. The tubes made of different alloys were located in neighboring rings and had a slight temperature difference (the difference in maximum temperatures was around 20 °C), which is much lower than the temperature difference at different elevations for the same rod. The main parameters of the samples are summarized in Table 3. The lengths of the hydrides were measured on binary metallographic images using GIMP software individually for each bundle elevation and the corresponding results are presented in Table A2 in the Appendix.

The statistical distribution of hydride lengths measured in this study is well described by a lognormal distribution. Typical examples of experimental histograms and fitted lognormal curves for both alloys are shown in Figs. 17 and 18. As seen in Fig. 17*a*, for the micrograph corresponding partial hydride dissolution, the hydride length histogram can be interpreted as the sum of three distributions, with local maximums at 25, 50, and 80 μm. One possible interpretation is that long hydrides result from the consolidation of two or three short hydrides, as evidenced by the multiple lengths. Nevertheless, the histogram can be described by a single lognormal curve with acceptable accuracy, which is used here for simplicity.

The lengths of the hydrides in Zircaloy-4 and opt. ZIRLO differ significantly. This discrepancy cannot be attributed to variations in local conditions within the bundle. Rather, it appears to be the result of differences in the texture and grain misorientation of these two alloys. These differences influence the grain boundary conditions and, consequently, the hydride nucleation process. As Fig. 19 shows, the length distribution in opt. ZIRLO is wider and shifted toward higher values than in Zircaloy-4. Fig. 19*b* shows the difference in length distribution in samples with complete hydride dissolution (to eliminate uncertainty caused by partially dissolved hydrides).

Based on Fig. 19 and Table A2, it can be concluded that the average and maximum lengths of the hydrides in the opt. ZIRLO are 2 – 3 times higher than those in Zircaloy-4 under similar conditions of slow cooling in samples with complete hydride dissolution (hydrogen concentration below 200 ppm). This difference in length may be due to the different densities of preferred hydride nucleation sites in these alloys, which are

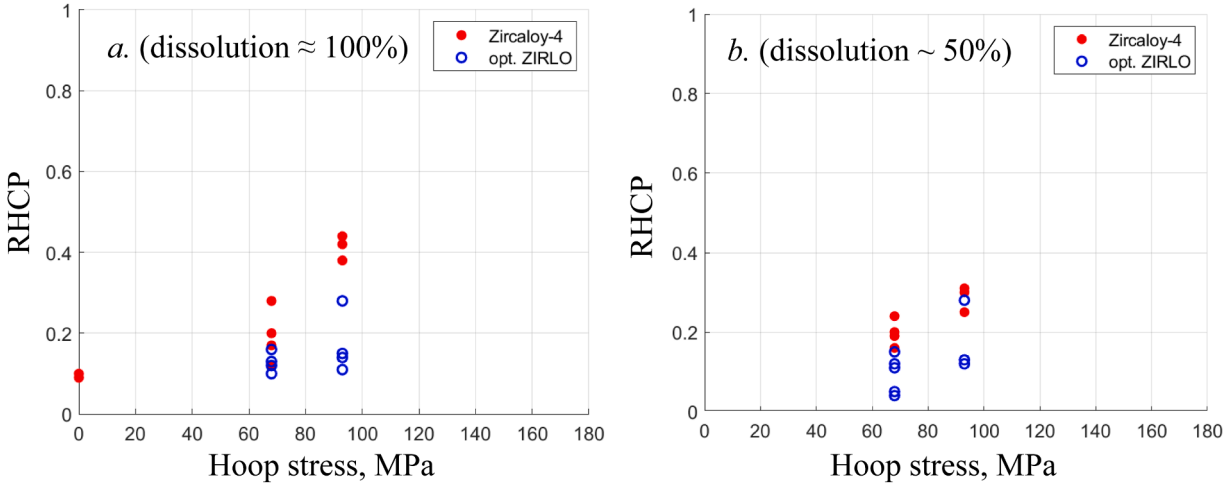

Fig. 15. A comparison of RHCP for Zircaloy-4 (red markers) and opt. ZIRLO (blue markers) measured after SPIZWURZ tests.

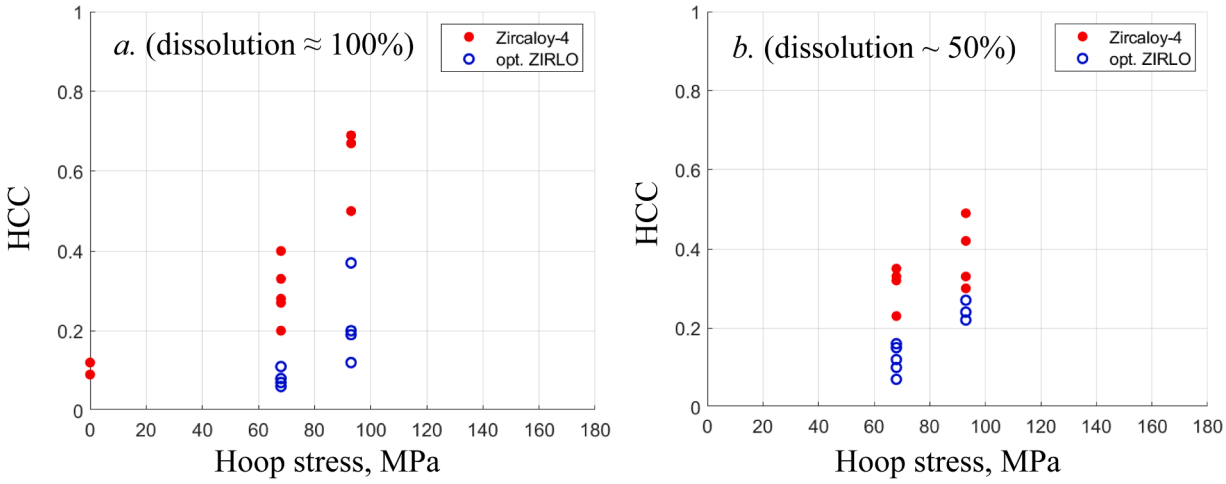

Fig. 16. A comparison of HCC for Zircaloy-4 (red markers) and opt. ZIRLO (blue markers) measured after SPIZWURZ tests.

Table 3
The main experimental conditions for the samples used in the hydride length analysis.

	Alloy	Target H concentration, ppm	Target internal pressure, bar	Bundle position
rod 2	Zircaloy-4	300	146	the second (middle) ring of tubes, max temp. 375 °C
rod 4		100	106	
rod 6		300	106	
rod 8		100	146	
rod 10	opt. ZIRLO	300	146	the third (outer) ring of tubes, max temp. 355 °C
rod 12		100	146	
rod 15		100	106	
rod 16		300	106	

caused by their different microstructures. During slow cooling, hydrogen atoms in the solid solution have enough time to reach the preferred nucleation sites and form hydrides with the lowest Gibbs energy. With faster cooling, hydrides nucleate at less preferred sites due to higher supersaturation, and the difference between the alloys may decrease. Consequently, the number density of hydrides is higher and the length is lower for faster cooling. This explains why the average hydride length and surface density are more pronounced in samples with low hydrogen concentrations where the initial morphology factor is excluded (Fig. 20*a* and 20*b*). The hydride morphology in samples with partial hydride dissolution (hydrogen concentration above 200 ppm) depends on the initial hydride morphology (before the bundle test begins), which forms during cooling after hydrogenating tubes at a cooling rate several orders of magnitude higher than in the bundle test. Note that the experimental points in Figs. 20*a* and 20*b* cannot be approximated by smooth correlations because the conditions for hydride nucleation at low and high concentrations are different, and the hypothetical correlation is expected to have a discontinuity at maximal solubility during the bundle test (approximately 200 ppm in the hottest axial zones).

The hydride length density characterizes the hydrogen concentration, which is described by a linear dependence (Fig. 21*a* and 21*b*). The parameters of this dependence for Zircaloy-4 and opt. ZIRLO are nearly identical within their margin of error.

An alternative calculation of RHF were made using the described hydride length statistic collected manually from eight rods. This calculation results were then compared to the results of the numerical automated method described in Chapter 3.1, which was applied to all rods.

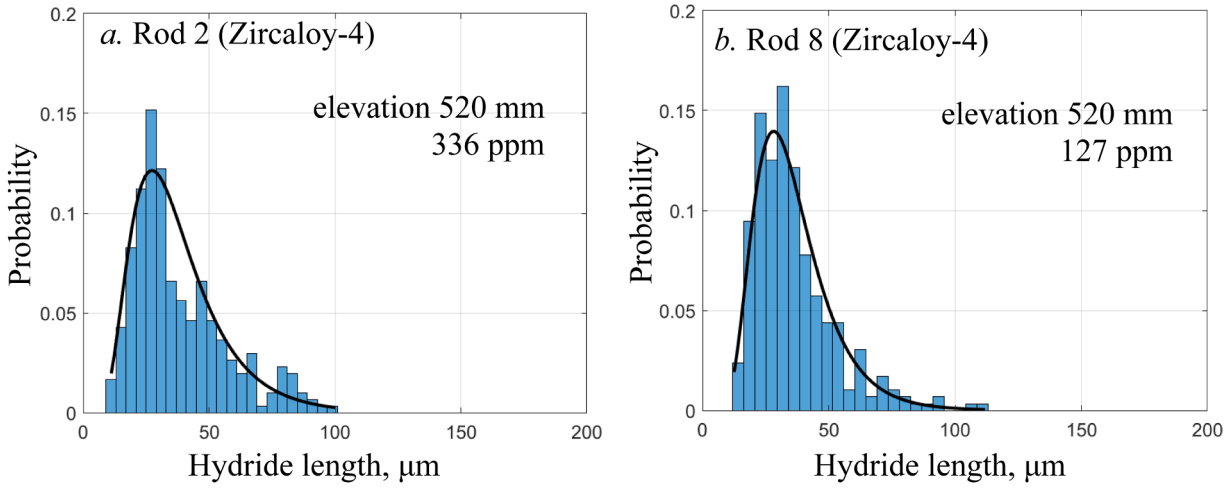

Fig. 17. A lognormal distribution of hydride lengths in Zircaloy-4 samples. Two examples are shown, one with partial (left) and one with complete (right) hydride dissolution during the test.

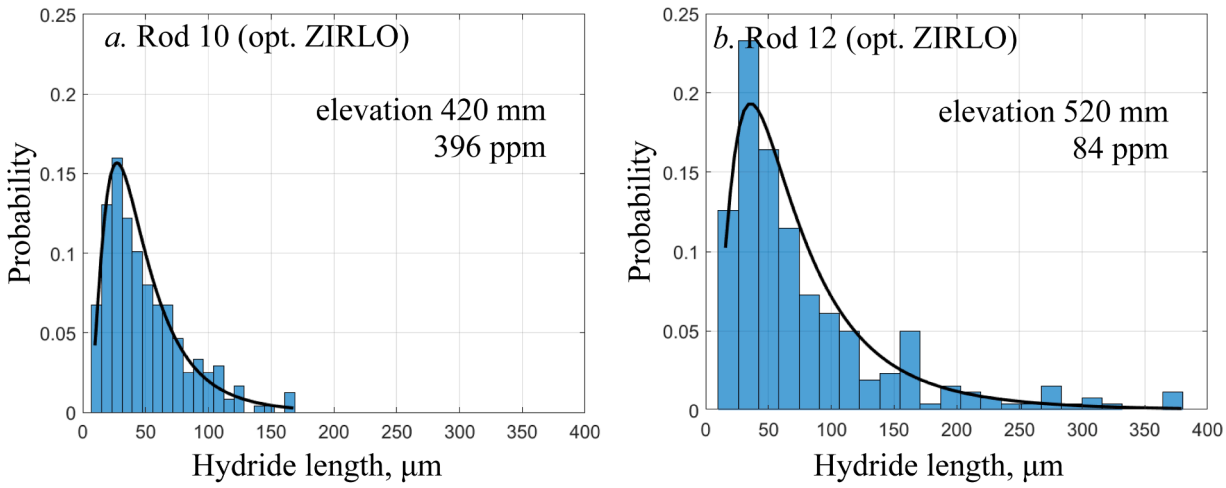

ProbabilityProbabilityFig. 18. A lognormal distribution of hydride lengths in opt. ZIRLO samples. Two examples are shown, one with partial (left) and one with complete (right) hydride dissolution during the test.

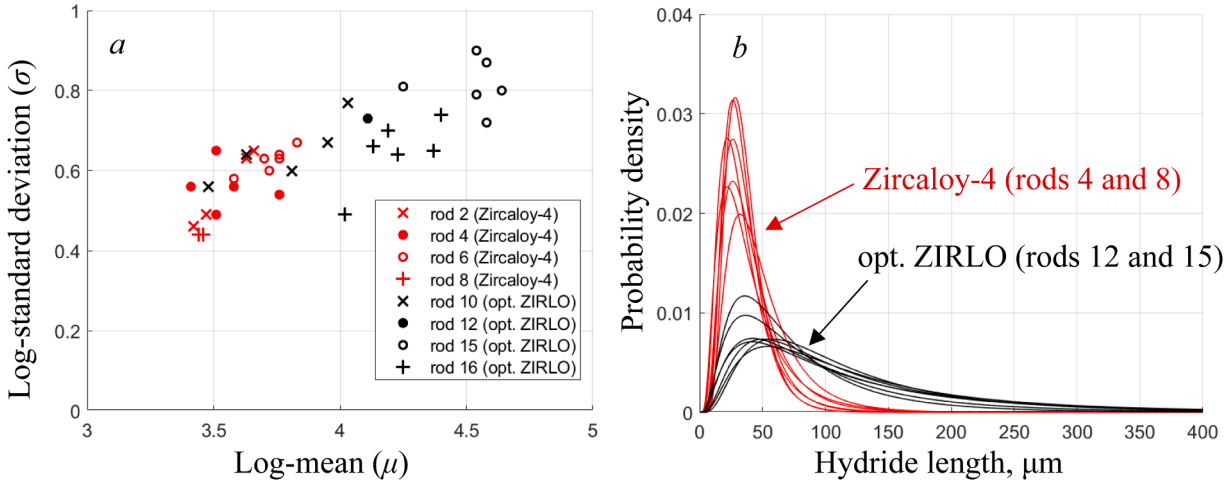

Fig. 19. The comparison parameters of the lognormal distribution of hydride lengths in Zircaloy-4 and opt. ZIRLO: *a* – scatter plot (all measured data), *b* – probability density of lengths (rods with complete hydride dissolution during the test).

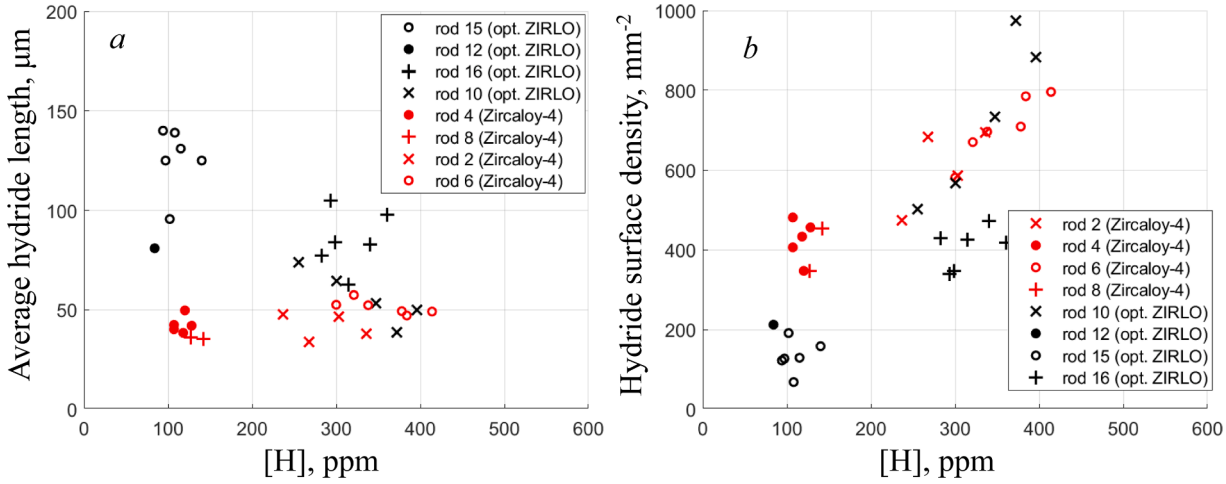

Fig. 20. The dependence of the average length and surface number density of the hydrides on the hydrogen concentration. A comparison of Zircaloy-4 (red) and opt. ZIRLO (black).

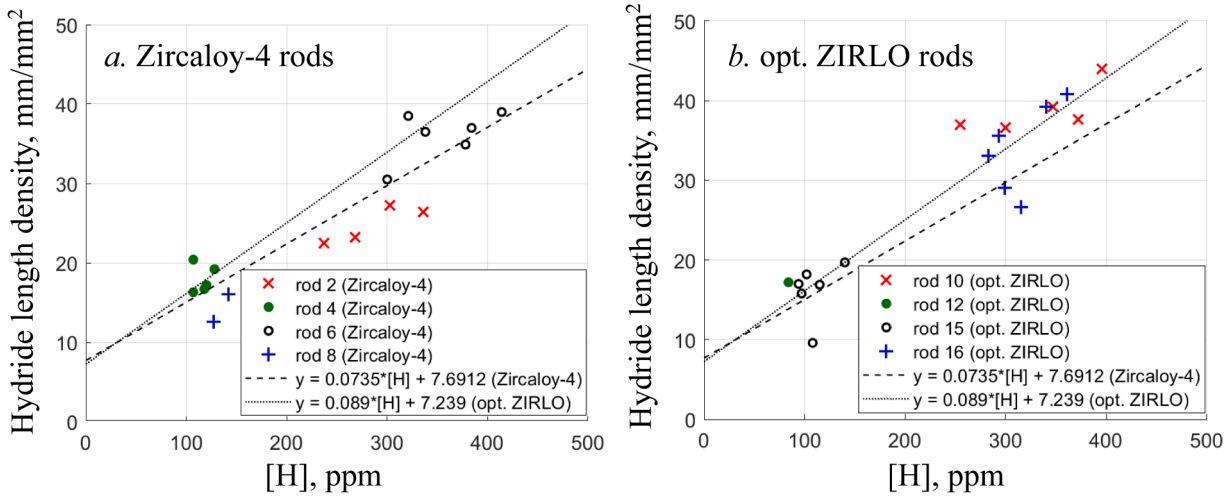

Fig. 21. Dependence of hydride length density on hydrogen concentration in Zircaloy-4 (left) and opt. ZIRLO (right).

This comparison was performed to validate and self-check the automated method. The results, which are considered acceptable, are shown in Figs. 22*a* and 22*b*

3.5. Hydride morphology in the duplex alloy DX-D4

Five of the cladding tubes in the bundle were manufactured from duplex DX-D4 alloy with an outer liner. Rods 1, 9, and 20 contained approximately 300 ppm of hydrogen, while rods 19 and 21 contained approximately 100 ppm. The presence of the liner significantly impacts the hydride morphology and redistribution throughout the cladding thickness. During holding at high temperature, the hydrogen in the substrate migrates to the liner/substrate interface. Consequently, most of the hydrogen accumulates at the interface and in the liner, as illustrated in Fig. 23. These results are consistent with published data [39,9,40]. The progressive dissolution of hydrides in the substrate that remained undissolved after heating is driven by the transport of hydrogen toward liner. Initially, a "hydride-depleted zone" forms in the substrate near the liner/substrate interface. This zone grows radially until it reaches the opposite surface, as seen in the hot zones at elevations 400–600 mm in Fig. 23. The different stages of the "hydride-depleted zone" can be seen in Fig. 23 and in publications [39,9,40]. The thickness of the "hydride-depleted zone" depends on the temperature and holding time, and it can be estimated approximately with simplified equations. Samples with approximately 100 ppm (rods 19 and 21) had uniform hydride morphology due to complete or nearly complete dissolution in all cross sections considered.

The problem can be formulated as determining the thickness of the hydride-depleted zone h_{hdz} as a function of the temperature scenario $T(\tau)$, which varies between different axial zones and tubes within the bundle. This problem is analogous to the classical Stefan problem (on the movement of phase boundary) of one-dimensional solidification from a supercooled melt [41]. The only difference is that the Stefan problem was solved for heat transfer and solidification, which requires tuning the equations. Based on Neumann's solution to the Stefan problem (see Section 3.2 in [41]), the thickness of the hydride-depleted zone increases with time as:

$$h_{hdz} = 2\lambda \cdot \sqrt{\int_0^t D_{\mathrm{H}}(T(\tau)) \cdot \mathrm{d}\tau} \tag{4}$$

D_{H} – hydrogen diffusion coefficient, λ – the non-dimensional coefficient depending on the hydrogen concentration and dissolution, which can be found from the following equation [41]:

$$\lambda e^{\lambda^2} \cdot \mathrm{erfc}(\lambda) = \frac{C_{ss} - C_{interface}}{C_{sub,tot} - C_{interface}} \cdot \frac{1}{\sqrt{\pi}} \tag{5}$$

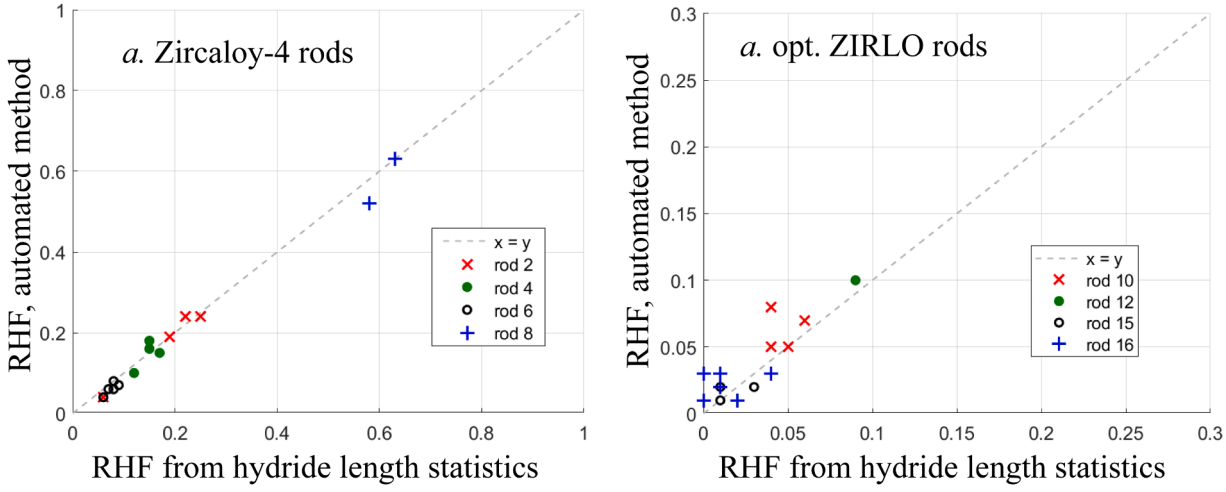

Fig. 22. A comparison of the RHF measured using two methods is presented: the automated procedure (with the numerical tool [25]) and the alternative procedure based on the hydride length statistic.

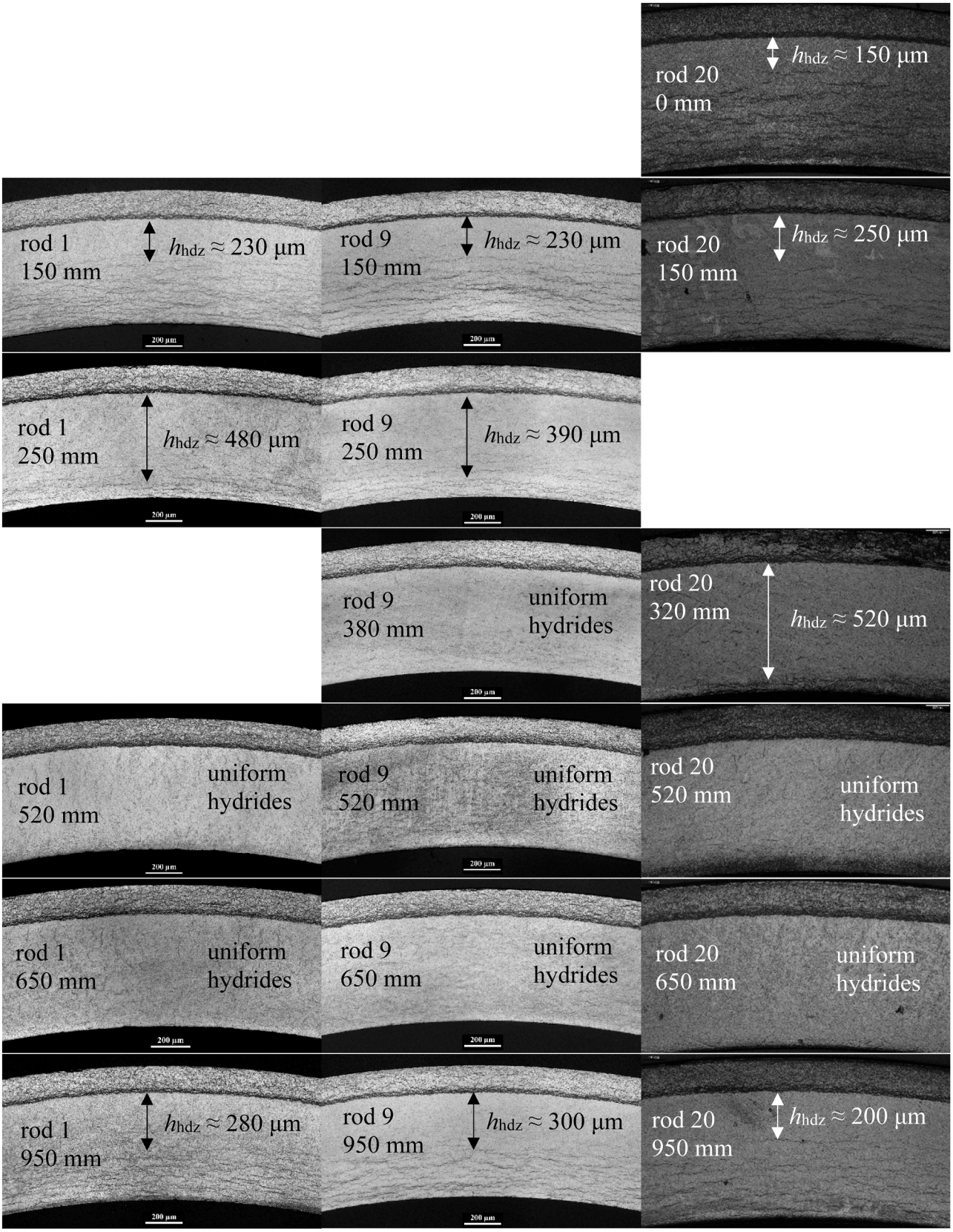

Fig. 23. Hydride-depleted zones in DX-D4 samples have a hydrogen concentration of approximately 300 ppm: left – rod 1, middle – rod 9, right – rod 20.

C_{ss} – hydrogen concentration in solid solution in the substrate, $C_{interface}$ – hydrogen concentration at the interface, $C_{sub,tot}$ – total initial hydrogen concentration in the substrate. The difference in hydrogen solubilities in the liner C_{liner} and substrate $C_{liner}/C_{ss} \approx \exp(-\Delta\mu_H/RT)$, where, $\Delta\mu_H$ – the difference of hydrogen chemical potential in substrate and liner, which was experimentally estimated in [9] to be equal to 656 [J/mol], which gives $C_{liner}/C_{ss} \approx 0.8 \div 0.9$ for the relevant temperatures. The estimation of λ for 300 ppm and 300 °C with Eq. (5) gives the typical value $\lambda \approx 0.01$, which is used for further calculations.

The results of the calculations using Eq. (4) with $D_H = 7.9{\cdot}10^{-7}{\cdot}\exp(-44{,}890/RT)$ [m^2/s] [42] are compared with the experimental data in Table 4. The Pearson correlation coefficient r between the experimental and calculated data was estimated to be 0.94 using the following equation:

$$r = \frac{\sum_i \left(h_{hdz,\exp,i} - \overline{h}_{hdz,\exp}\right)\left(h_{hdz,\mathrm{calc},i} - \overline{h}_{hdz,\mathrm{calc}}\right)}{\sqrt{\sum_i \left(h_{hdz,\exp,i} - \overline{h}_{hdz,\exp}\right)^2}\cdot\sqrt{\sum_i \left(h_{hdz,\mathrm{calc},i} - \overline{h}_{hdz,\mathrm{calc}}\right)^2}} \quad (6)$$

where $h_{hdz,\exp}$ and $h_{hdz,\mathrm{calc}}$ correspond to the hydride-depleted zones measured in the experiments and calculated using Eq. (4), respectively.

The results of the experiment–calculation comparison presented in Table 4 can be considered acceptable when taking into account both the complexity of the physical processes involved and the simplicity of Eq. (4). In reality, hydrogen redistribution is governed by two-phase diffusion, initially non-uniform radial and axial hydrogen distributions, as well as precipitation and redissolution of hydrides during temperature drops during shutdowns. Despite significant simplification of the model, the obtained results show good correlation with the experimental data. Therefore, the model can be applied for rapid, approximate estimations of the time required for complete hydrogen redistribution from the substrate, or for assessing whether a given temperature scenario will result in such redistribution.

Thermodynamic equilibrium in claddings with a liner is expected when all of the hydrides in the substrate are dissolved and the hydrogen concentration in the solid solution of the substrate is in equilibrium ("uniform hydrides" in Fig. 23). During subsequent cooling, the remaining hydrogen in the substrate can diffuse partially into the liner and partially precipitate in the substrate as hydrides. The fractions of hydrogen that diffuse to the liner and that precipitate in the substrate are determined by the balance of hydrogen flow to the liner and by supersaturation growth in the substrate due to cooling. This balance (and the amount of precipitated hydrides) is governed by the cooling rate. The nucleation of hydrides in the substrate during cooling is expected to be similar to that in Zircaloy-4, adjusted to the actual substrate concentration. This is confirmed by comparing RHF in hot zones for DX-D4 and Zircaloy-4, with complete hydride dissolution (Fig. 24). The DX-D4 experimental data has wide scatter due to the low number of hydrides in the cross-section and the uncertain actual substrate hydrogen concentration after cooling.

Table 4
Thickness of the hydride-depleted zone in DX-D4 rods with 300 ppm (target).

	elevation, mm	[H], ppm	highest T, °C	hydride depleted zone thickness, μm	
				experiment	calc., Eq. (4)
rod 1	150	307	300	230	390
	250	286	350	480	570
	520	315	400	> 575*	800
	650	304	390	> 575*	750
	950	300	250	280	270
rod 9	150	273	290	230	360
	250	274	340	390	536
	380	264	370	> 575*	660
	520	292	390	> 575*	715
	650	314	380	> 575*	715
	950	292	200	300	182
rod 20	0	282	180	150	130
	150	274	280	250	340
	320	268	360	520	600
	520	282	370	> 575*	660
	650	305	360	> 575*	621
	950	326	200	200	180

* – samples with uniform hydride distribution in the substrate (the hydride depleted zone is equal to the substrate thickness = 575 μm).

3.6. Inhomogeneity of hydride morphology

Micrograph analysis of the samples used in SPIZWURZ revealed a few anomalies in the local hydride morphology (among more than one hundred cross-sections of all twenty-one samples). The first type of anomaly is relatively long, radially oriented hydrides, as shown in Figs. 25 and 26. The second type of anomaly is a significant local RHF inhomogeneity, as shown in Fig. 27. Although these inhomogeneities in hydride morphology are relatively rare and can be found only in a small percentage of samples, they can seriously degrade local properties and play a crucial role in cladding fracture.

4. Conclusion

The hydride morphology was thoroughly and detailly investigated after the SPIZWURZ bundle test, which simulated the dry storage of spent nuclear fuel. The micrographs examined correspond to zones with varying hydrogen concentrations (80 – 400 ppm), internal gas pressures (106, 146 bar), maximum temperatures (150 – 400 °C), and alloys (Zircaloy-4, opt. ZIRLO, and DX-D4). The following conclusions can be formulated:

- the hydrogen adsorption rate from the gas mixture was around two times higher in Zircaloy-4 than in the opt. ZIRLO. One possible explanation is that Laves phases create "windows" on the surface that favor hydrogen adsorption; however, the exact physical mechanism remains unclear,
- unirradiated Zircaloy-4 samples have a higher RHF, RHCP and HCC than opt. ZIRLO under similar conditions. The RHF, RHCP and HCC of both alloys increases with external stresses. The measured RHF for Zircaloy-4 and opt. ZIRLO is consistent with the published data;
- both the mean and maximum hydride lengths in the opt. ZIRLO are two to three times longer than those in Zircaloy-4 under similar conditions. Accordingly, the hydride number density in opt. ZIRLO is

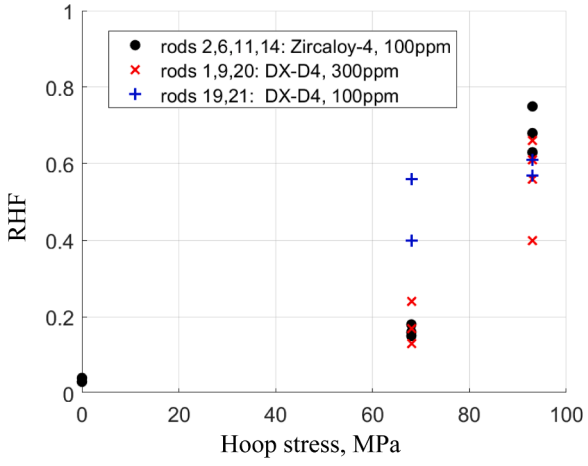

Fig. 24. RHF in hot zones (350 – 700 mm) in Zircaloy-4 with complete dissolution of hydrides (black dots) and in substrate of DX-D4 alloy (other markers).

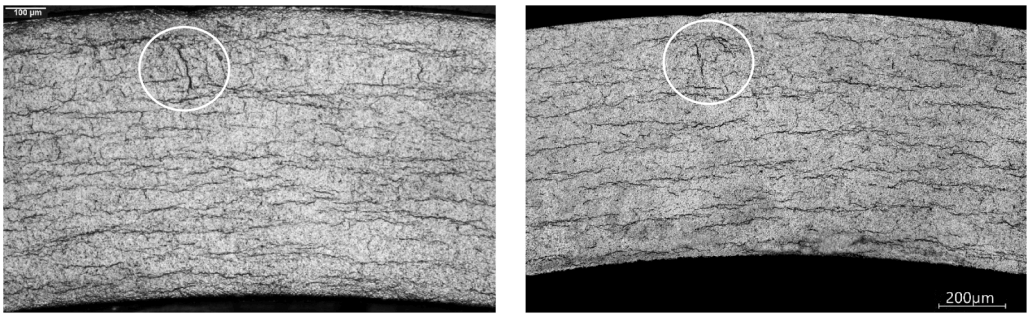

Fig. 25. Inhomogeneous hydride morphology. Single radial hydride anomaly.

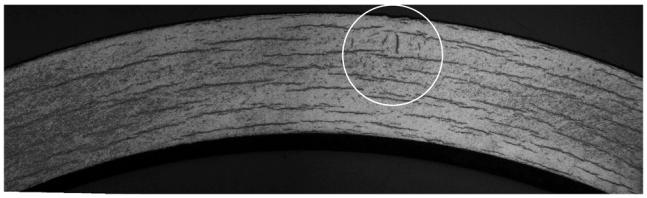

Fig. 26. Inhomogeneous hydride morphology. Single radial hydride anomaly: rod 13 (elevation 950 mm, the mean RHF = 0.03).

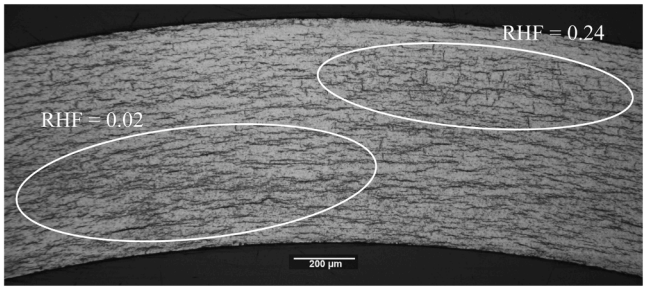

Fig. 27. Inhomogeneous hydride morphology. Anomaly inhomogeneity of RHF in rod 7 (elevation 150 mm, the mean RHF = 0.07).

lower than that in Zircaloy-4. The hydride length density per unit area is similar in both alloys and is proportional to the total hydrogen concentration;

- in the Duplex alloy DX-D4, after heating, hydrogen diffuses from the substrate to the liner. This process can be accompanied by hydride dissolution in the substrate and their subsequent precipitation at the boundary and in the liner. The RHF in the DX-D4 substrate is similar to that in Zircaloy-4, allowing for the actual hydrogen concentration after redistribution;
- several samples exhibited local anomalies in hydride morphology. These anomalies could significantly increase the degree of local hydride embrittlement and play a significant role in the fracture process;

CRediT authorship contribution statement

Mikhail Kolesnik: Writing – original draft, Visualization, Investigation, Formal analysis, Data curation. **Juri Stuckert:** Writing – review & editing, Supervision, Project administration. **Mirco Grosse:** Writing – review & editing, Funding acquisition. **Sarah Weick:** Writing – review & editing, Data curation.

Declaration of competing interest

The authors declare that they have no known competing financial interests or personal relationships that could have appeared to influence the work reported in this paper.

Acknowledgement

The SPIZWURZ project (FKZ RS1586A/1501609B) is funded by the Federal Ministry for the Environment, Nature Conservation, Nuclear Safety and Consumer Protection (BMUV). The authors thank KIT/INE and GRS as project partners and the fruitful discussions in the preparation of the test. Particularly, we thank Aleksandra Rezchikova for organizing the benchmark activities and the analysis of the results.

The authors are grateful to all KIT colleagues involving in the preparation and conducting of the test as well as in the post-test evaluations of the claddings. In particular, the authors would like to thank Jürgen Moch and Conrado Rössger for assembly and disassembly of the test bundle, Ursula Peters, Conrado Rössger and Julia Lorentz for the preparation of the post-tests samples and the metallographic investigations.

Supplementary materials

Supplementary material associated with this article can be found, in the online version, at doi:10.1016/j.jnucmat.2025.156250.

Appendix. Collected hydride morphology data

Table A1
Experimental results of the SPIZWURZ bundle test. Hydride morphology metrics RHF, RHCP and HCC.

Rod	Cladding material	H concentration	Inner pressure	Elevation, mm	Angle, °	RHF	RHCP	HCC
1	DUPLEX (substrate)	C_{max}	P_{max}	150	180	**0.17**	**0.40**	**0.40**
				250	135	**0.23**	**0.23**	**0.22**
				520	345	**0.66**	**0.34**	**0.35**
				650	30	**0.61**	**0.40**	**0.45**
				950	270	**0.25**	**0.37**	**0.31**
2	Zircaloy-4	C_{max}	P_{max}	−50	0	**0.04**	**0.12**	**0.12**
				150	135	**0.19**	**0.26**	**0.34**
				380	180	**0.24**	**0.30**	**0.30**
				520	0	**0.24**	**0.31**	**0.33**
				650	0	**0.27***	**0.30***	**0.49***
				950	180	**0.14***	**0.20***	**0.18***
3	opt. ZIRLO	C_{min}	P_{max}	150	—	**0.12**	**0.13**	**0.18**
				350	—	**0.14**	**0.14**	**0.12**
				520	—	**0.19**	**0.28**	**0.37**
				650	—	**0.12**	**0.15**	**0.19**
				850	—	**0.13**	**0.14**	**0.16**
				1050	—	**0.15**	**0.15**	**0.29**
4	Zircaloy-4	C_{min}	P_{min}	150	0	**0.11***	**0.12***	**0.21***
				250	135	**0.10**	**0.20**	**0.29**
				380	225	**0.15**	**0.28**	**0.33**
				520	45	**0.18**	**0.20**	**0.28**
				650	90	**0.16**	**0.20**	**0.27**
				950	250	**0.15**	**0.24**	**0.28**
5	opt. ZIRLO	C_{max}	P_{min}	150	90	**0.02**	**0.09**	**0.18**
				250	185	**0.01**	**0.13**	**0.08**
				380	125	**0.01**	**0.12**	**0.10**
				520	180	**0.02**	**0.11**	**0.12**
				650	295	**0.02**	**0.15**	**0.15**
				950	225	**0.02**	**0.11**	**0.08**
6	Zircaloy-4	C_{max}	P_{min}	150	0	**0.06**	**0.15**	**0.21**
				250	0	**0.06**	**0.14**	**0.18**
				380	30	**0.08**	**0.24**	**0.33**
				520	0	**0.07**	**0.20**	**0.35**
				650	0	**0.06**	**0.19**	**0.23**
				950	180	**0.04**	**0.15**	**0.24**
7	opt. ZIRLO	C_{max}	P_{max}	150	0	**0.07**	**0.21**	**0.31**
				250	90	**0.03**	**0.17**	**0.09**
				520	0	**0.08**	**0.28**	**0.27**
				950	135	**0.06**	**0.17**	**0.17**
8	Zircaloy-4	C_{min}	P_{max}	150	0	**0.52***	**0.44***	**0.48***
				250	270	**0.66***	**0.41***	**0.67***
				380	270	**0.75***	**0.38***	**0.50***
				520	0	**0.63**	**0.42**	**0.69**
				650	45	**0.68**	**0.44**	**0.67***
				950	180	**0.52**	**0.36**	**0.64**
9	DUPLEX (substrate)	C_{max}	P_{min}	150	315	**0.06**	**0.14**	**0.12**
				250	180	**0.06**	**0.10**	**0.10**
				380	135	**0.17**	**0.19**	**0.23**
				520	120	**0.24***	**0.17***	**0.23***
				650	350	**0.13**	**0.12**	**0.22**
				950	0	**0.05**	**0.09**	**0.12**
10	opt. ZIRLO	C_{max}	P_{max}	0	45	**0.07**	**0.17**	**0.26**
				150	45	**0.05**	**0.15**	**0.23**
				320	180	**0.08**	**0.13**	**0.22**
				420	270	**0.05**	**0.12**	**0.24**
				650	270	**0.08**	**0.13**	**0.22**
11	Zircaloy-4	C_{max}	P_{max}	520	180	**0.21**	**0.25**	**0.42**
12	opt. ZIRLO	C_{min}	P_{max}	520	112	**0.10**	**0.11**	**0.20**
13	opt. ZIRLO	C_{min}	P_{min}	250	180	**0.02**	**0.10**	**0.07**
				380	90	**0.02**	**0.12**	**0.11**
				520	135	**0.03***	**0.16***	**0.11***
				650	0	**0.01**	**0.12**	**0.08**
				950	135	**0.09**	**0.23**	**0.20**
					225	**0.03**	**0.12**	**0.06**
14	Zircaloy-4	C_{min}	P_{min}	150	135	**0.15**	**0.16**	**0.22**
				250	180	**0.12***	**0.13***	**0.24***
				380	45	**0.16**	**0.12**	**0.27**
				520	330	**0.15**	**0.17**	**0.20**
				650	90	**0.18**	**0.17**	**0.40**
				950	180	**0.08***	**0.11***	**0.13***
15	opt. ZIRLO	C_{min}	P_{min}	150	90	**0.02**	**0.11**	**0.14**

(*continued on next page*)

Table A1 (*continued*)

Rod	Cladding material	H concentration	Inner pressure	Elevation, mm	Angle, °	RHF	RHCP	HCC
				250	135	**0.01**	**0.13**	**0.09**
				380	0	**0.01**	**0.10**	**0.07**
				520	0	**0.01**	**0.13**	**0.06**
				650	270	**0.02**	**0.12**	**0.11**
				950	315	**0.01**	**0.06**	**0.03**
16	opt. ZIRLO	C_{max}	P_{min}	250	0	**0.02**	**0.05**	**0.09**
				380	270	**0.03**	**0.12**	**0.16**
				520	0	**0.01**	**0.04**	**0.10**
				650	180	**0.01**	**0.05**	**0.07**
				800	270	**0.03**	**0.14**	**0.10**
				950	270	**0.03**	**0.11**	**0.10**
17	Zircaloy-4	C_{max}	P_{min}	250	270	**0.08**	**0.14**	**0.19**
				520	315	**0.10**	**0.16**	**0.32**
				950	90	**0.09**	**0.16**	**0.16**
18	Zircaloy-4	C_{min}	1 bar	150	154	**0.04**	**0.08**	**0.10**
				380	325	**0.04**	**0.10**	**0.12**
				520	130	**0.03**	**0.09**	**0.09**
				950	325	**0.06**	**0.08**	**0.11**
19	DUPLEX (subsrate)	C_{min}	P_{min}	250	155	**0.09**	**0.12**	**0.12**
				380	130	**0.13***	**0.10***	**0.16***
				520	320	**0.11**	**0.14**	**0.15**
				650	315	**0.12**	**0.20**	**0.26**
				950	150	**0.08**	**0.15**	**0.21**
20	DUPLEX (substrate)	C_{max}	P_{max}	0	225	**0.18***	**0.21***	**0.20***
				150	180	**0.09**	**0.13**	**0.13**
				320	0	**0.29**	**0.13**	**0.23**
				520	225	**0.40**	**0.28**	**0.23**
				650	225	**0.56***	**0.27***	**0.32***
				950	225	**0.12**	**0.16**	**0.17**
21	DUPLEX (substrate)	C_{min}	P_{max}	150	235	**0.19**	**0.34**	**0.27**
				250	160	**0.26**	**0.33**	**0.39**
				380	65	**0.57**	**0.42**	**0.37**
				520	0	**0.61**	**0.29**	**0.45**
				650	345	**0.61**	**0.31**	**0.41**
				950	125	**0.23**	**0.19**	**0.25**

* rough estimation due to over-etched sample.

Table A2
Experimental results of the SPIZWURZ bundle test. Length of hydrides.

Rod	Clad. material	Inner press., bar	Elevat. mm	Angle, grad.	[H] conc., ppm.	Max. length, μm		Mean length, μm			param. of lognormal distr.		Length density, mm/mm^2	2D hyd. dens, mm^{-2}	RHF (from h. length)
						all	rad.	all	rad.	circ.	μ	σ			
2	Zircaloy-4	146	−50	0	237	**170**	**39.9**	**47.5**	**16.7**	**53.6**	**3.66**	**0.65**	**22.5**	**473**	**0.06**
			150	135	303	**222**	**132**	**46.4**	**25.5**	**57.1**	**3.63**	**0.63**	**27.2**	**586**	**0.19**
			380	180	268	**112**	**59.4**	**34.0**	**22.5**	**39.8**	**3.42**	**0.46**	**23.2**	**683**	**0.22**
			520	0	336	**100**	**49.7**	**38.0**	**26.0**	**45.1**	**3.47**	**0.49**	**26.4**	**694**	**0.25**
			650	0	334	—	—	—	—	—	—	—	—	—	—
			950	180	347	—	—	—	—	—	—	—	—	—	—
4	Zircaloy-4	106	150	0	109	—	—	—	—	—	—	—	—	—	—
			250	135	107	**178**	**53.6**	**42.4**	**22.7**	**48.4**	**3.58**	**0.56**	**20.4**	**481**	**0.12**
			380	225	107	**175**	**41.8**	**40.2**	**20.9**	**50.1**	**3.41**	**0.56**	**16.3**	**406**	**0.17**
			520	45	120	**216**	**57.7**	**49.7**	**27.2**	**58.6**	**3.76**	**0.54**	**17.2**	**347**	**0.15**
			650	90	118	**136**	**61.1**	**38.4**	**24.3**	**42.8**	**3.51**	**0.49**	**16.7**	**433**	**0.15**
			950	250	128	**229**	**60.3**	**42.0**	**23.3**	**50.3**	**3.51**	**0.65**	**19.2**	**456**	**0.17**
6	Zircaloy-4	106	150	0	338	**209**	**28.5**	**52.3**	**20.2**	**60.7**	**3.76**	**0.63**	**36.5**	**696**	**0.08**
			250	0	321	**225**	**33.5**	**57.4**	**19.6**	**66.5**	**3.83**	**0.67**	**38.5**	**670**	**0.07**
			380	30	384	**166**	**37.7**	**47.1**	**17.8**	**54.9**	**3.58**	**0.58**	**37.0**	**785**	**0.08**
			520	0	414	**139**	**37.7**	**49.1**	**19.9**	**57.0**	**3.72**	**0.60**	**39.0**	**796**	**0.09**
			650	0	378	**178**	**36.8**	**49.3**	**19.4**	**56.6**	**3.70**	**0.63**	**34.9**	**709**	**0.08**
			950	180	300	**189**	**36.8**	**52.5**	**19.7**	**59.0**	**3.76**	**0.64**	**30.5**	**581**	**0.06**
8	Zircaloy-4	146	150	0	113	—	—	—	—	—	—	—	—	—	—
			250	270	111	—	—	—	—	—	—	—	—	—	—
			380	270	118	—	—	—	—	—	—	—	—	—	—
			520	0	127	**112**	**112**	**36.2**	**37.3**	**34.6**	**3.46**	**0.44**	**12.6**	**346**	**0.63**
			650	45	123	—	—	—	—	—	—	—	—	—	—
			950	180	142	**115**	**103**	**35.3**	**30.6**	**44.9**	**3.44**	**0.44**	**16.0**	**453**	**0.58**
10	opt. ZIRLO	146	0	45	372	**159**	**33.6**	**38.6**	**18.9**	**41.4**	**3.48**	**0.56**	**37.6**	**974**	**0.06**
			150	45	347	**170**	**32.2**	**53.4**	**19.5**	**57.8**	**3.81**	**0.6**	**39.2**	**734**	**0.04**
			320	180	300	**240**	**47.6**	**64.3**	**20.4**	**70.1**	**3.95**	**0.67**	**36.6**	**568**	**0.04**
			420	270	396	**168**	**47.8**	**49.8**	**18.5**	**54.4**	**3.63**	**0.64**	**44.0**	**884**	**0.05**
			650	270	255	**317**	**44.4**	**73.7**	**18.7**	**84.1**	**4.03**	**0.77**	**37.0**	**502**	**0.04**

(*continued on next page*)

Table A2 (*continued*)

Rod	Clad. material	Inner press., bar	Elevat. mm	Angle, grad.	[H] conc., ppm.	Max. length, μm		Mean length, μm			param. of lognormal distr.		Length density, mm/mm^2	2D hyd. dens, mm^{-2}	RHF (from h. length)
						all	rad.	all	rad.	circ.	μ	σ			
12	opt. ZIRLO	146	150	—	94	—	—	—	—	—	—	—	—	—	—
			250	—	101	—	—	—	—	—	—	—	—	—	—
			380	—	97	—	—	—	—	—	—	—	—	—	—
			520	112	84	**379**	**46.5**	**80.9**	**27.7**	**99.1**	**4.11**	**0.73**	**17.2**	**212**	**0.09**
			650	—	103	—	—	—	—	—	—	—	—	—	—
			950	—	127	—	—	—	—	—	—	—	—	—	—
15	opt. ZIRLO	106	150	90	102	**360**	**53.3**	**95.6**	**22.4**	**108**	**4.25**	**0.81**	**18.2**	**191**	**0.03**
			250	135	115	**620**	**30.4**	**131**	**22.4**	**140**	**4.58**	**0.87**	**16.9**	**129**	**0.01**
			380	0	94	**517**	**45.7**	**140**	**26.6**	**144**	**4.64**	**0.80**	**17.0**	**122**	**0.01**
			520	0	140	**641**	**59.8**	**125**	**28.4**	**129**	**4.58**	**0.72**	**19.7**	**158**	**0.01**
			650	270	97	**608**	**32.6**	**125**	**20.8**	**131**	**4.54**	**0.79**	**15.8**	**127**	**0.01**
			950	315	108	**663**	**34.8**	**139**	**27.4**	**146**	**4.54**	**0.90**	**9.5**	**68**	**0.01**
16	opt. ZIRLO	106	250	0	299	**301**	**29.3**	**83.8**	**18.7**	**87.8**	**4.23**	**0.64**	**29.1**	**347**	**0.01**
			380	270	283	**319**	**48.0**	**77.2**	**24.7**	**84.1**	**4.13**	**0.66**	**33.1**	**429**	**0.04**
			520	0	361	**468**	**20.4**	**97.8**	**17.9**	**98.9**	**4.37**	**0.65**	**40.8**	**417**	**0.00**
			650	180	315	**249**	**32.0**	**62.5**	**20.6**	**64.7**	**4.02**	**0.49**	**26.6**	**426**	**0.02**
			800	270	340	**316**	**15.7**	**82.9**	**13.8**	**85.1**	**4.19**	**0.70**	**39.2**	**472**	**0.00**
			950	270	293	**410**	**22.7**	**105**	**18.0**	**108**	**4.40**	**0.74**	**35.6**	**339**	**0.01**

Data availability

Data will be made available on request.

References

[1] R. Sedláček, D. Deuble, Self-compensation in creep of pressurized cladding tubes: from self-limitation in dry storage to self-acceleration in burst tests, Nucl. Eng. Des. 413 (2023) 112480, https://doi.org/10.1016/j.nucengdes.2023.112480. April.

[2] P. Konarski, C. Cozzo, G. Khvostov, H. Ferroukhi, Spent nuclear fuel in dry storage conditions – current trends in fuel performance modeling, J. Nucl. Mater. 555 (2021) 153138, https://doi.org/10.1016/j.jnucmat.2021.153138.

[3] P.A.C. Raynaud, R.E. Einziger, Cladding stress during extended storage of high burnup spent nuclear fuel, J. Nucl. Mater. 464 (2015) 304–312, https://doi.org/10.1016/j.jnucmat.2015.05.008.

[4] M.P. Puls, The Effect of Hydrogen and Hydrides on the Integrity of Zirconium Alloy Components, Springer-Verlag, London, 2012.

[5] A.T. Motta, et al., Hydrogen in zirconium alloys: a review, J. Nucl. Mater. 518 (2019) 440–460, https://doi.org/10.1016/j.jnucmat.2019.02.042.

[6] M. Grosse, et al., The SPIZWURZ project – Experimental investigations and modeling of the behavior of hydrogen in zirconium alloys under long-term dry storage conditions, Nucl. Eng. Technol. 56 (2024) 824–831, https://doi.org/10.1016/j.net.2023.09.027.

[7] S. Weick et al., "The SPIZWURZ project - experimental and modeling approaches of hydrogen in cladding tubes under dry storage conditions," 2024, doi:10.1115/ICONE31-136905.

[8] O. Yetik, P. Trtik, R. Zubler, R.M. Grabherr, J. Bertsch, L.I. Duarte, Hydrogen redistribution in non-irradiated and irradiated duplex zirconium claddings by high-resolution neutron imaging, J. Nucl. Mater. (2024) 155780, https://doi.org/10.1016/j.jnucmat.2025.155780 no. (to be submitted.

[9] W. Gong, et al., Hydrogen diffusion and precipitation in duplex zirconium nuclear fuel cladding quantified by high-resolution neutron imaging, J. Nucl. Mater. 526 (2019) 151757, https://doi.org/10.1016/j.jnucmat.2019.151757.

[10] U.S. Nuclear Regulatory Commission, "Spent Fuel Project Office Interim Staff Guidance - 11, Revision 3," 2003.

[11] J. Stuckert, C. Rössger, J. Moch, M. Grosse, and S. Weick, "Hydrogenation of claddings in the new developed HOKI oven and performance of the long-term bundle test under dry storage conditions in the framework of the SPIZWURZ project," 2023, doi:10.5445/IR/1000168767.

[12] C.E.L. Hunt, E.M. Schulson, Recrystallization of Zircaloy-4 during transient heating, J. Nucl. Mater. 92 (1980) 184–190, https://doi.org/10.1016/0022-3115(80)90101-4.

[13] S. Kim, D. Son, J.H. Kang, Y. Lee, Recrystallization and grain growth of Zr-Nb-Sn alloy in 400–500 °C and effect on hydride embrittlement, J. Nucl. Mater. 583 (2023) 154477, https://doi.org/10.1016/j.jnucmat.2023.154477. February.

[14] S. Naito, Kinetics of hydrogen absorption by α-zirconium, J. Chem. Phys. 79 (6) (1983) 3113–3120, https://doi.org/10.1063/1.446142.

[15] X.F. Wang, et al., Kinetics of hydrogen absorption/desorption in the Zr-2.5Nb alloy, Phys. Chem. Chem. Phys. 26 (26) (2024) 18196–18204, https://doi.org/10.1039/d4cp01512f.

[16] D.G. Ivey, D. Northwood, Storing hydrogen in AB2 laves-type compounds*, Zeitschrift für Phys. Chemie Neue Folge 147 (1986) 191–209, https://doi.org/10.1524/zpch.1986.147.1.

[17] R.M. Van Essen, K.H.J. Buschow, Hydrogen absorption in various based intermetallic compounds, J. Less-Common Met. 64 (1979) 277–284, https://doi.org/10.1016/0022-5088(79)90178-4.

[18] C. Jones, et al., Evidence of hydrogen trapping at second phase particles in zirconium alloys, Sci. Rep. (2021) 1–12, https://doi.org/10.1038/s41598-021-83859-w.

[19] G. Kuri, H. Ramanantoanina, J. Bertsch, M. Martin, I. Panas, Chemical state and atomic scale environment of nickel in the corrosion layer of irradiated Zircaloy-2 at a burn-up around 45 MWd/kg, Corros. Sci. 143 (2018) 200–211, https://doi.org/10.1016/j.corsci.2018.08.032. July.

[20] F. Stein, G. Sauthoff, M. Palm, Experimental determination of intermetallic phases, phase equilibria, and invariant reaction temperatures in the Fe-Zr system, J. Phase Equilibria 23 (6) (2002) 480–494, https://doi.org/10.1361/105497102770331172.

[21] K. Xiao, L. Zhou, X. Kong, D. Luo, J. Song, Hydrogen interaction with Mn-doped Zr2Fe (101) surface : a DFT study, Int. J. Hydrogen Energy 47 (48) (2022) 20932–20941, https://doi.org/10.1016/j.ijhydene.2022.04.203.

[22] P.A. Burr, S.T. Murphy, S.C. Lumley, M.R. Wenman, R.W. Grimes, Hydrogen solubility in zirconium intermetallic second phase particles, J. Nucl. Mater. 443 (1–3) (2013) 502–506, https://doi.org/10.1016/j.jnucmat.2013.07.060.

[23] B. Cox, Zirconium Intermetallics and Hydrogen Uptake During Corrosion, Chalk River, Ontario, 1987 [Online]. Available: https://inis.iaea.org/records/3245h-4fa91.

[24] Standard specification for wrought zirconium alloy seamless tubes for nuclear reactor fuel cladding, ASTM Int (2022), https://doi.org/10.1520/B0811-13R22E01 vol. B811-13.

[25] P.C.A. Simon, C. Frank, L.Q. Chen, M.R. Daymond, M.R. Tonks, A.T. Motta, Quantifying the effect of hydride microstructure on zirconium alloys embrittlement using image analysis, J. Nucl. Mater. 547 (2021) 152817, https://doi.org/10.1016/j.jnucmat.2021.152817.

[26] L.G. Bell, R.G. Duncan, Hydride Orientation in Zr-2.5% Nb; How It is Affected By stress, Temperature and Heat Treatment, Pinawa, Manitoba, Canada, 1975.

[27] M. Nakatsuka, S. Yagnik, Effect of hydrides on mechanical properties and failure morphology of BWR fuel cladding at very high strain rate, J. ASTM Int. 8 (1) (2010), https://doi.org/10.1520/JAI102954 p. Paper ID JA102954.

[28] Q. Auzoux, et al., Hydride reorientation and its impact on mechanical properties of high burn-up and unirradiated cold-worked stress-relieved Zircaloy-4 and ZirloTM fuel cladding, J. Nucl. Mater. 494 (2022) 153893, https://doi.org/10.1016/j.jnucmat.2022.153893.

[29] J. Desquines, C. Sartoris, M. Guémas, A. Gérard, Radial hydride precipitation in fuel cladding during back-end cooling transient under decreasing pressure, in: Water Reactor Fuel Performance Meeting, WRFPM 2023, 2023, pp. 80–86, https://doi.org/10.1007/978-981-99-7157-2_8.

[30] H.C. Chu, S.K. Wu, R.C. Kuo, Hydride reorientation in Zircaloy-4 cladding, J. Nucl. Mater. 373 (1–3) (2008) 319–327, https://doi.org/10.1016/j.jnucmat.2007.06.012.

[31] Y.J. Kim, D.H. Kook, T.H. Kim, J.S. Kim, Stress and temperature-dependent hydride reorientation of Zircaloy-4 cladding and its effect on the ductility degradation, J. Nucl. Sci. Technol. 52 (5) (2014) 717–727, https://doi.org/10.1080/00223131.2014.978829.

[32] R.S. Daum, S. Majumdar, Y. Liu, M.C. Billone, Radial-hydride embrittlement of high-burnup zircaloy-4 fuel cladding, J. Nucl. Sci. Technol. 43 (9) (2006) 1054–1067, https://doi.org/10.1080/18811248.2006.9711195.

[33] K.N. Jang, K.T. Kim, The effect of neutron irradiation on hydride reorientation and mechanical property degradation of zirconium alloy cladding, Nucl. Eng. Technol. 49 (7) (2017) 1472–1482, https://doi.org/10.1016/j.net.2017.05.006.
[34] P. Bouffioux, et al., Hydride reorientation in M5® cladding and its impact on mechanical properties, in: LWR Fuel Perform. Meet. Top Fuel 2013 2, 2013, pp. 879–886.
[35] R.A. Kurskii, et al., Reorientation of hydrides in unirradiated clad tubes made of alloy E110 under conditions simulating long-term dry storage of spent nuclear fuel, Phys. Met. Metallogr. 122 (9) (2021) 861–868, https://doi.org/10.1134/S0031918×21090076.
[36] R.A. Kurskii, et al., Evolution of the hydride structure in irradiated E110 alloy in the process of thermomechanical treatment simulating supercritical dry storage conditions, Izv. Wysshikh Uchebnykh Zawedeniy, Yad. Energ. (In Russ. 2023 (1) (2023) 108–120, https://doi.org/10.26583/npe.2023.1.09.
[37] A.-M. Alvarez, et al., On the effect of internal pressure and cooling rate on the hydride reorientation in optimized ZIRLO cladding, in: TopFuel 2024, 2024, 29 September–3 October.
[38] D. Woo, Y. Lee, Understanding the mechanical integrity of Zircaloy cladding with various radial and circumferential hydride morphologies via image analysis, J. Nucl. Mater. 584 (2023) 154560, https://doi.org/10.1016/j.jnucmat.2023.154560. June.
[39] Q. Auzoux, et al., Hydride reorientation and its impact on ambient temperature mechanical properties of high burn-up irradiated and unirradiated recrystallized Zircaloy-2 nuclear fuel cladding with an inner liner, J. Nucl. Mater. 494 (2017) 114–126, https://doi.org/10.1016/j.jnucmat.2017.07.022.
[40] A.-M. Alvarez, et al., Evaluation of the hydride reorientation behavior for Zircaloy-2 liner cladding with high hydrogen content during interim dry storage conditions, Zircon. Nucl. Ind. 20th Int. Symp. (2023) 673–694, https://doi.org/10.1520/stp164520220013.
[41] J. Crank, Free and Moving Boundary Problems, Clarendon Press, Oxford, 1984.
[42] J.J. Kearns, Diffusion coefficient of hydrogen in alpha zirconium, Zircaloy-2 and Zircaloy-4, J. Nucl. Mater. 43 (3) (1972) 330–338, https://doi.org/10.1016/0022-3115(72)90065-7.